STRUCTURAL STABILITY OF MEMS ARCHES ACTUATED BY ELECTROSTATIC FRINGING FIELDS

BY
TAUSIFF FIRAQUE MOHAMMAD

A Thesis Presented to the
DEANSHIP OF GRADUATE STUDIES

KING FAHD UNIVERSITY OF PETROLEUM & MINERALS

DHAHRAN, SAUDI ARABIA

In Partial Fulfillment of the
Requirements for the Degree of

MASTER OF SCIENCE

In

MECHANICAL ENGINEERING

MAY 2014

KING FAHD UNIVERSITY OF PETROLEUM & MINERALS
DHAHRAN- 31261, SAUDI ARABIA
DEANSHIP OF GRADUATE STUDIES

This thesis, written by **TAUSIFF FIRAQUE MOHAMMAD** under the direction his thesis advisor and approved by his thesis committee, has been presented and accepted by the Dean of Graduate Studies, in partial fulfillment of the requirements for the degree of **MASTER OF SCIENCE IN MECHANICAL ENGINEERING.**

Zuhair Gasem
Dr. ZUHAIR GASEM
Department Chairman

Dr. Salam A. Zummo
Dean of Graduate Studies

27/5/14
Date

THESIS COMMITTEE

HASSEN OUAKAD May 18th 2014
Dr. HASSEN OUAKAD
(Advisor)

M. Hawwa
Dr. MUHAMMAD HAWWA
(Member)

H. Qahtani
Dr. HUSSAIN AL-QAHTANI
(Member)

Dedication

To my parents, Mohammad Talim and Ashmara Begum, and my beloved brother Ashiff.

ACKNOWLEDGMENTS

First and foremost, I would like to express my highest gratitude to Almighty ALLAH, the most merciful the most gracious, for this achievement. I thank him for giving me life, knowledge and making my MS program a success.

I thank my advisor Dr. Hassen Ouakad for his continuous guidance and direction in this research work. This thesis would not have been possible without it. I express my appreciation to Dr. Muhammad Hawwa and Dr. Hussain Al-Qahtani to be a part of my evaluation committee and for their fruitful suggestions.

I would also like to thank all my KFUPM graduate colleagues and friends who helped me in one way or the other. I thank Mr. Asim Ghaffar, Mr. Binash Imteyaz and Mr. Rio Turnadi for helping me whenever I needed anything from them. Thanks to my friends Imil Hamda Imran, Fahim Jatmika, Fahrudin Muna, Bagus Susilo, Younus Siddiqui, Madhar Sahib and Mohamed Yunus for their love and affection.

My hearty gratitude goes to my father, Mohammad Talim, for his innumerable sacrifices and struggles and vast patience to make me reach this stage of qualification and success. My heartfelt thankfulness goes to my mother, Ashmara Begum, for her abundant love, care and prayer throughout my life. I express my appreciation to my beloved brother, Ashiff, for his support and encouragements.

TABLE OF CONTENTS

LIST OF FIGURES

LIST OF TABLES

ABSTRACT

Full Name : TAUSIFF FIRAQUE MOHAMMAD

Thesis Title : STRUCTURAL STABILITY OF MEMS ARCHES ACTUATED BY ELECTROSTASTIC FRINGING FIELDS.

Major Field : MECHANICAL ENGINEERING

Date of Degree : MAY 2014

In this thesis, we investigate a micro-electromechanical system (MEMS) arch microbeam actuated by fringing electric field where the electrodes are located at both side of the microbeam. An electrostatic force caused by asymmetry of the fringing electric fields acts in a direction opposite to the relative deflection of the microbeam, resulting in a restoring electrostatic force which increasing with the applied DC voltage. A reduced-order model (ROM) is derived for the considered system using the so-called Galerkin decomposition and assuming linear undamped mode shapes of a straight beam as base functions in the decomposition process. A static analysis is performed to investigate the occurrence of the snap-through instability. The eigenvalue problem is then investigated to obtain the fundamental as well as higher natural frequencies variation of the microbeam with the applied DC load. A bifurcation analysis is then implemented to derive a criterion for whether symmetric or asymmetric bifurcation is occurring during the static snap-through instability. The results show elimination of the so-called pull-in instability in this kind of systems as the stationary electrodes are located on either sides rather than at the bottom as in case parallel plate actuation. This system can be useful to design pull-in free MEMS bi-stable devices.

ملخص الرسالة

الاسم الكامل: توصيف فيرق محمد

عنوان الرسالة: ثبات البناء للميمس المقوسة والمشغلة بواسطة حقول مجنبة من الكهرباء الساكنة

التخصص: الهندسة الميكانيكية

تاريخ الدرجة العلمية: مايو 2014

في هذه الرسالة, سيتم دراسة نوع من أنظمة المايكرو التي تستخدم الكهرباء وتعتمد على حركة ميكانيكية أو مايسمى(بالميمس). هذا النوع يستخدم عامود مقوس في حجم المايكرو ومشغل بواسطة حقل كهربائي مجنب, حيث الأقطاب الكهربائية تقع على طرفي العامود. قوة الكهرباء الساكنة تتولد من عدم التطابق الحاصل في الحقول الكهربائية المجنبة والتي تعمل في الاتجاه المعاكس للانحراف النسبي للعامود, مما يؤدي إلى استعادة قوة الكهرباء الساكنة والتي تزيد عند التزويد بالجهد المباشر. تم إيجاد نموذج الدرجة المخفضة لهذا النظام باستخدام طريقة جالركين بافتراض وضعية الأشكال للنظام الخطي الغير واهن للعامود المستقيم كدوال أساسية عند الاشتقاق. وتم عمل كذلك تحليل البيانات لوضعية الثبات لفحص حدوث عدم الاستقرار عند ظاهرة الاعوجاج للأسفل. ومن ثم تم إيجاد القيم الذاتية لإيجاد اهتزاز التردد الرئيسي وكذلك الاهتزاز لترددات ذي درجات أعلى تحت تأثير حمل ثابت. أيضا تم عمل دراسة التشعيب لاشتقاق معيار لرؤية ما إذا كان التشعيب متطابق أو غير متطابق خلال ظاهرة الاعوجاج للأسفل عند الحمل الثابت. النتائج أظهرت اختفاء لما يسمى بظاهرة الالتصاق للداخل لهذه النوعيات من النظم التي تجعل الأقطاب الكهربائية الثابتة تقع على الجنب بدلا من أن تكون بأسفلها مباشرة. لهذا نستطيع القول بأن هذه النوعية من النظم مفيدة عندما يتطلب تصميم أجهزة ميمس مستقرة و خالية من ظاهرة الانجذاب الداخلي.

CHAPTER 1

INTRODUCTION

1.1 Motivation

Microelectromechanical systems (MEMS) devices have a wide range of applications thanks to their small size, cheap mass production and low power requirement for operations. MEMS are used as resonators, filters, pressure sensors, accelerometers [2], controllers for micro-mirrors [3], micro-pumps [4], inductors [5], Bio-MEMS [6], etc. Although MEMS have been commercialized in a variety of areas, new phenomenon and interesting behavior are being discovered to date. This suggests that there is a lot of scope for research in the MEMS community and to harness its potential for possibly new applications and with more improvements in the existing areas.

Microbeam based structure employed in several MEMS devices are micrometer scaled devices and represents one of the most used structures in the MEMS industry. Cantilever or clamped-clamped microbeams form the basic structural component of numerous MEMS devices. They can be used as atomic microscope probes [7, 8], switching elements in RF capacitive micro-switches [9, 10], resonant sensors [11] and RF filters [12]. Microbeams can also be employed as spring elements in other MEMS structures such as comb drive actuators [13, 14].

Curved microbeams (also known as arches) are clamped-clamped microbeams formed initially with a parabola, a circle or a sine function. It has been the focus of research recently due to their bi-stability nature [15-17]. They do not require power to remain in the actuated position. Power is required only for transition from one stable configuration to another. It is one of the most important structures when low power consuming devices are needed. It can have large displacement as opposed to straight perfectly clamped-clamped beam which are mainly mono-stable devices. Arches do not require a permanent axial force to be formed, which is difficult to control. Curved microbeams have been used as micro-switches [18], mechanical storage devices [19] and biomedical actuators [20].

Snap through motion is an important phenomenon in the arch structural behavior which can be used in various switching and actuation applications. During snap through motion [21] the arch exhibits a sudden jump flipping to a new stable position in a symmetrically opposite configuration. The arches can vibrate around its initial curved shape or around its symmetrically opposite position. It can also vibrate with large amplitude between the two symmetrically opposite positions by exhibiting snap through. This snap-through motion has been utilized to produce various MEMS devices like artificial muscle actuators [22], robotic manipulators and MEMS relays [23, 24].

Electrostatic actuation is one of the commonly used techniques for driving microbeams based actuators. Although parallel plates electrostatically actuated arches [25] is the most used method in a lot of applications, MEMS engineers and designers are turning their focus to fringing field electrostatic actuation method. In this latter configuration the electrodes are located at the sides of the microbeam and not at the bottom in case of the parallel plate electrostatic actuation. Elimination of the pull-in instability found in parallel plate electrostatic actuation is one of the prime factors for considering this type of actuation. Unlike parallel plate actuation, the dependence of electrostatic force is not monotonic in case of fringing field electrodes. The electrostatic force is present due to asymmetry of the curvature of the beam and acts as a restoring force. The behavior is different than the mechanical equivalent loading of the arches due to non-linearity of the deflection dependent electrostatic force such as the one discussed in [1, 25]. In this configuration the net force goes to zero when the beam becomes straight. Researchers have focused in fringing field electrostatic actuation recently for mainly designing new variety of sensors and actuators. This fringing field actuation technique mostly works in a non-contact basis and thus avoiding instabilities like pull-in [26, 27] and stiction. Hence this may results in increase in the life of the device with large displacement amplitude.

Therefore studying the statics and dynamics of the fringing field actuated curved micro beams may reveal many new behavior and phenomenon. These features may help in designing new devices which are of unique characteristics in the MEMS world or even to overcome some of the current deficiencies in some MEMS devices.

1.2 Literature Review

1.2.1 Electrostatically Actuated Curved Microbeams

Krylov et al. [1], Zhang et al. [28] were among few groups who investigated the snap through and pull in instabilities of arch shaped microbeams actuated electrostatically. Ouakad and Younis [29] studied the static response of MEMS arch actuated by electric DC load. They [29] also studied the dynamic behavior of shallow arch by superimposing DC load on an AC harmonic load both theoretically as well as experimentally. They showed that the snap-through and pull-in depends on the initial configuration of the arch. Krylov and Dick [30] investigated the transient dynamics of the initially curved clamped-

clamped microbeam reporting its dynamic snap through and pull in. Das and Batra [31] studied the pull-in and snap-through instabilities in MEMS arches under time-dependent electric potential difference. They showed that depending on the rate of applied electrical loading the micro arch may exhibit snap-through and pull-in or only pull-in without snap-through. Younis et. al. [32] discussed the non-linear dynamics of curved micro beams actuated by harmonic electrostatic load and presented primary as well as secondary (super-harmonic and sub-harmonic) resonances. Batra et. al. [33, 34] have used local Petrov-Galerkin (MLPG) and also Finite Element (FE) methods to model the mechanical behavior of electrically actuated narrow micro beams microbeams. Nonlinear equations of MLPG and FE were solved using Displacement Iteration Pull-In Extraction (DIPIE). 3-D modeling of FE was done using finite element code ANSYS.

1.2.2 Fringing Field Electrostatic Actuation

Hah et al. [35] developed a hybrid with angular vertical comb-drive (AVC) and angular vertical comb-drive (AVC) micro mirrors for doing their parametric study. The hybrid model calculates the capacitance between the fingers of the comb drive with a 2-D finite element model considering the fringing field effect. They found that the fringe fields have an important contribution in the calculation of the micro mirrors' maximum rotation angles. Agache et al. [36] performed an Atomic Force Microscope (AFM) characterization of out-of-plane fixed-fixed MEMS resonators with high frequency in a non-contact mode. He and Ben Mrad [37] developed analytically a model for a repulsive-force actuator to predict its force and the maximum out-of plane displacement. They conducted numerical simulations to verify the model. They also developed experimentally a repulsive-force rotation micro mirror to verify their model.

Lee [38] modeled a new type of non-contact electrostatic micro actuator with slit structures which have nonlinear electrostatic force acting on the stationary electrodes and the movable structure. He provided a closed form equation for the nonlinear electrostatic force on the movable structure determining its coefficients with finite element analysis (FEA) and dimensional analysis. The coefficients in the equation depend on the geometrical properties of the micro actuator. He also proposed that there is pull-in and pull-out phenomenon observed only if the movable grating is above a minimum height. There is no mechanical contact during pull-in or pull-out because the electrodes are on the sides and not on the bottom. Neither pull-in nor pull-out is observed if the height is lee than this minimum value. This value of minimum height depends on the geometry of the micro actuator. This can help to produce devices where pull-in and pull-out is required or not and avoiding mechanical contact which results in collapse.

Su et al. [39] discussed a useful offset-drive method to fabricate the electrodes at an offset position in the lateral direction instead of exactly below. The adopted configuration prevents direct contact of the electrodes and avoids any possibilities of pull-in. Actuation occurs due to fringing field rather than parallel plate actuation. They also proposed an offset electrode capacitance model which shows that the lateral gap has to be greater than a critical value to avoid pull-in. Linzon et al. [40] performed experimental and theoretical analysis of microcantilevers actuated by fringing field electrostatics to obtain large amplitude displacements without the limitation of stiction with the electrodes. Krylov et al. [41] have modeled curved microbeams which are actuated by electrodes located out of the plane. This has eliminated pull-in instabilities of closed gap actuation. In fringing field actuation of curved beams snap-through may or may not occur depending on the initial elevation and voltage.

1.2.3 Reduced Order Model (ROM)

There are several techniques to discretize the non-linear partial differential equation of beam. Reduced order model (ROM) [42, 43] is one of most commonly used method for discretization of the beam equations in MEMS research.

Younis et al. [44] devised a new reduced order model technique using Galerkin procedure to obtain a finite-degree of freedom system consisting of ordinary-differential equation in time. First few base linear-undamped mode shapes of the beam were used as the base functions in the Galerkin procedure. The reduced order model needs very few mode shapes to converge which saves the computation cost and time considerably. Whereas the conventional numerical methods solving boundary value problem which may not converge or suffer from stiffness of equations at the unstable regions. Nayfeh et al. [45] did a classification study of the ROMs for the MEMS device. They divided it into node method and domain method. The node method evaluates the equations in the discretization mesh at each node to obtain the system matrices. The domain method uses Galerkin method and modal analysis to obtain the equation in terms of modes or eigenfunctions. The domain method is further divided into two parts. The first type uses the finite element method (FEM) or finite difference method (FDM) to obtain the time series of the full non-linear model. The basis set extracted from this time series is then used in the Galerkin procedure. The second type of domain method is using the mode shapes of the system in the Galerkin procedure. This process gives a proper behavior of the device both qualitatively and quantitatively and performs well with nonlinearities when sufficient numbers of modes are used. They used this second category to develop ROMs for micro beams and different types of micro plates. They also used ROM to model thermo elastic damping and squeeze-film damping in MEMS. Yuming et al. [46] have used ROM to model magnetically actuated micro beams. They took into account the coupling between the beam deflection and the magnetic force. Linear mode shapes of the micro beam were used as base functions for ROM.

1.2.4 Snap Through and Symmetry Breaking

Arch microbeams with high initial mid-point elevation may exhibit symmetric breaking instead of normal snap through at the point of bifurcation. The beam profiles along the length are asymmetric about the mid-span of the arch in the bifurcation region.

Pippard [47] and Patricio et al. [48] have studied the criteria of snap through of the arch loaded by quasistatic mechanical point load experimentally as well as numerically. Zhang et al. [28] and Krylov et al. [25] have discussed the static analysis of circular and bell shaped arches respectively undergoing snap through and pull in instabilities. Zhang et al. [28] suggested that the pull in and the snap through instabilities can be differentiated physically by observing whether there is contact between the arch and the fixed electrode. Krylov et al. [49] showed the relation between the initial midpoint elevation and the thickness of the microbeam for the occurrence of snap through in the static deflection of the arch.

The snap-through and the symmetry breaking criteria of curved beams with mechanical loading are well documented in Dym [49] and Simitses [50]. Pelesko et al. [51], Batra et al. [52] considered the asymmetrically occurrence of pull-in configurations in annular plates and membranes. Unlike mechanically actuated beam, electrostatically loaded beams deflection depends not only on the beam geometric nonlinearity but also on the electrostatic nonlinearity in addition [1].

Das and Batra [53] studied the symmetry breaking problem of an arch microbeam. They concluded that for arch beams with small elevations there is snap-through for static loading and there is symmetry about the arch mid-span, whereas for arches with large midpoint elevations they showed possibilities of symmetric breaking. They solved numerically using the Galerkin method the nonlinear partial differential governing equation of the transient deformations of the arch.

Medina et al. [54, 55] performed a bifurcation analysis for curved microbeams actuated electrostatically by parallel plates to obtain the criterion of symmetric and asymmetric bifurcation in terms of the geometric parameters of the beams. They considered various cases of loading starting with the simple case of uniform mechanical loading. They also considered the case of distributed nonlinear deflection-dependent electrostatic force applied to a stress free initially curved micro beam and also applied to a pre-stressed buckled beam due to axial load. They used reduced order model (ROM) obtained from the Galerkin decomposition while considering the buckling or vibrational modes of a straight beam used as the base functions.

1.3 Thesis Objectives and Organization

The objectives of this thesis are the following:

- To perform the static analysis of clamped-clamped curved micro beam actuated by electrostatic fringing field of electrodes located at either sides of the beam.

- To solve the eigenvalue problem of curved micro beam arch mentioned above and obtain the natural frequencies and mode shapes as function of applied DC load.
- To develop a bifurcation analysis of curved micro beam arch mentioned above to obtain a criterion for the initiation of symmetric and asymmetric bifurcation.
- To carry out a parametric study for the above mentioned cases for various arch's initial midpoint elevation.

The rest of this thesis will be organized as follows. In Chapter 2, we will discuss the differences of parallel plates and fringing field electrostatic actuation techniques. In Chapter 3, the model of the arch microbeam used in this work is presented. In the following chapters we present the results and discussions of the work. This will include the static analysis with only DC voltage actuation in chapter 4, eigenvalue analysis to investigate the variation of natural frequencies and mode shapes in chapter 5, and chapter 6 contains the bifurcation analysis of the arch to get the criterion of symmetric and asymmetric bifurcations. In Chapter 7, we summarize our work outcomes and present some recommendations for future research.

CHAPTER 2

BACKGROUND

2.1 Parallel Plate Electrostatic Actuation

The electrostatic actuation technique in MEMS is one of the commonly used actuation method because of its low consumption of power, fast actuation and the possibility of the integration into a standard integrated circuit. An electrically actuated system consists of an upper moving electrode (straight or curved) made of a conductive material placed above a fixed conductive electrode, Figure 2.1. The gap between the two is filled with a dielectric medium, usually air. When there is electric potential difference applied between the upper electrode and the fixed one, there is creation of an attractive electrostatic force between them. The moving electrode deflection towards the fixed electrode induces the restoring elastic forces of the structure of the microbeam which balances the Coulomb electric force. The electrostatic force is inversely proportional to the gap between the microbeam and the bottom electrode and increases with the deflection of the moving electrode [56]. This defection of the moving electrode continues to increase with the increase in the applied voltage until the restoring elastic force balances the electrostatic force. When there is further increase in the voltage, the elastic force can no more balance the Coulomb force causing the moving electrode to collapse to the bottom electrode resulting in the so called pull in instability [27, 57].

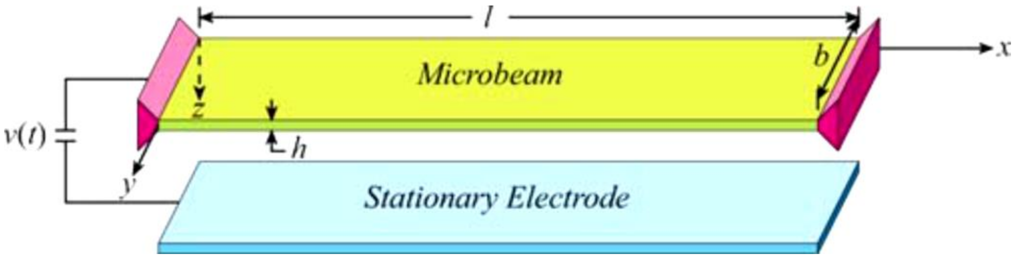

Figure 2.1: Schematic of a microbeam actuated by a parallel plate electrostatic field [45].

2.1.1 Electrostatic Force

The electrostatic force between two parallel plates assuming the electric field lines to be perpendicular to the plates and neglecting the fringing effects near the edges of the plates can be derived as follows:

We let the applied voltage be V, the electrical charge Q and potential energy stored in each capacitor

$$Q = C(z)V, \qquad E = \frac{V^2}{2}C(z), \tag{2.1}$$

where $C(z)$ is the capacitance between the two plates, Figure 2.2.

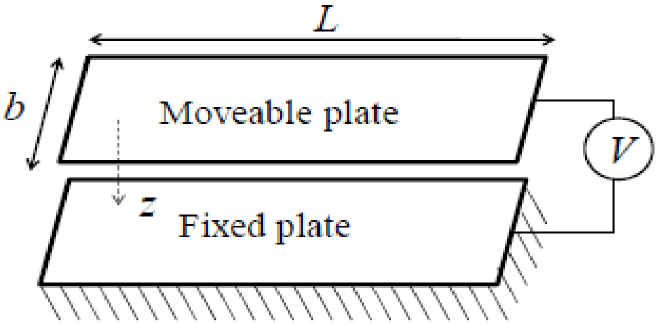

Figure 2.2: Schematic of a parallel plate capacitor [58].

The electrostatic force of attraction between the two plates is (Hayt and Buck [56]):

$$F_e = \frac{-\delta E(z)}{\delta z} = \frac{-V^2}{2}\frac{\delta C(z)}{\delta z}, \tag{2.2}$$

The capacitance of the rectangular parallel plate is (Hayt and Buck [56]):

$$C(z) = \frac{\varepsilon_0 Lb}{z}, \tag{2.3}$$

where ε_0 is the air permittivity.

Hence the electrostatic force is

$$F_e = \frac{-\varepsilon_0 LbV^2}{2z^2}, \tag{2.4}$$

2.1.2 The Pull In Instability

When there is voltage difference between the lower fixed electrode and the upper movable electrode (microbeam) of V_{DC} in parallel plate electrostatic actuation the microbeam deflects towards the bottom electrode. When the DC electrostatic load V_{DC} is small the beam remains in the deflected position as balanced by the opposing elastic restoring force of the microbeam. With further increase in V_{DC} at a particular value the elastic restoring force can no longer balance the Coulomb force. This leads to sudden movement of the microbeam to the lower electrode due to the attractive electrostatic force causing stiction and collapse of the device. This phenomenon is known as pull in instability [27, 57] and the value of V_{DC} at which this occurs is known as pull in voltage and the corresponding value of midpoint or peak deflection is called pull in displacement,

Figure 2.3. Typically, this DC load has a softening effect on the microbeam decreasing its linear natural frequency [59].

$V_{DC} = 0$ $V_{DC} > 0$ $V_{DC} \geq V_{Pull-in}$

Figure 2.3: Pull in instability in parallel plate electrostatic actuation.

2.2 The Snap Through Instability in Curved Structures

To illustrate the snap through instability in curved structures, we will use the below bifurcation diagram in Figure 2.4 which has two stable branches AC and DF. Initially, with the increase in the force, the curved structure deflection increases gradually from point A to point C. In this branch, the curved structure retains approximately its initial shape, and the applied force is balanced by the elastic force of the structure which is restoring in nature. When the deflection reaches point C, there is a sudden jump in the deflection and the structure reaches another new equilibrium position which is inverted to the initial curvature of the structure corresponding to point E. This is known as the snap through instability, Figure 2.5, and the corresponding load at which this occurs is the snap through force. The force is again balanced by the restoring elastic force of the structure from point E to point F. When the midpoint deflection reaches the point F curved microbeam instantly collapses on to the fixed electrode undergoing pull-in. Branches CD and FG are the unstable portions of the curve. The microbeam follows the path ACEFL and the path FDBA during loading and unloading respectively [31].

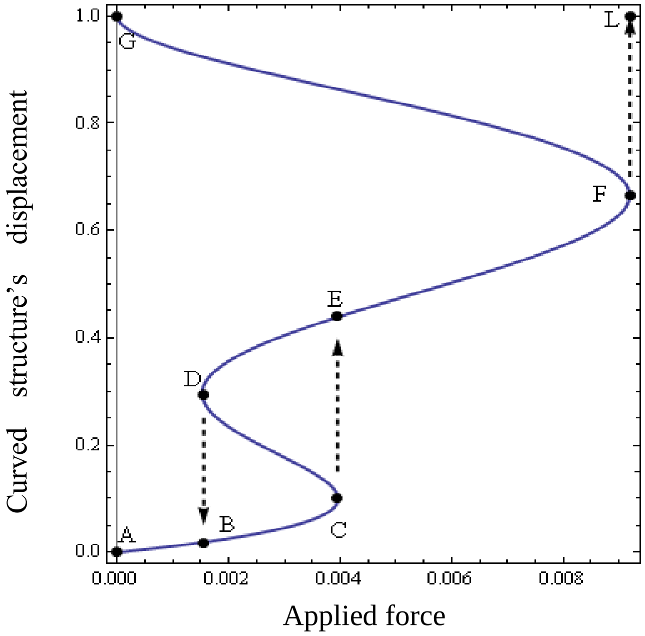

Figure 2.4: Snap through and pull in instabilities in the bifurcation diagram curved MEMS structure [1]

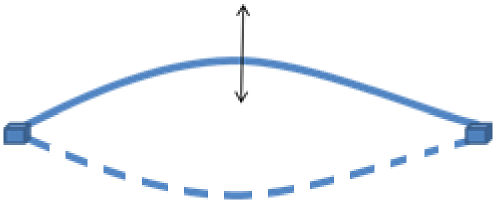

Figure 2.5: Snap through instability in curved MEMS structure

The snap through instability of the arch does not always occur. It depends on various parameters such as the initial midpoint elevation of the curved structure, its thickness, the gap between the fixed and the movable electrode and the type of loading (ramp or step). The three scenarios which can arise for an arch actuated by parallel plate electrostatics are as follows: occurrence of pull in only, snap through and pull in occurring one after the other or there is occurrence of snap through and pull in for the arch simultaneously. The pull in occurs in all cases.

2.3 Fringing Field Electrostatic Actuation

We consider here a clamped-clamped structure with electrodes located symmetrically at the two sides of it. The electrostatic force is applied by asymmetric distribution of electric fields due to the curvature of the microbeam. The direction of the Coulomb force is opposite to the curvature of the structure. The net electrostatic force is zero for a straight electrode as the distribution of the electric field is symmetric. The electrodes can be kept much smaller than the length of the curved microbeam to obtain almost uniform distribution of the electric field throughout the moving electrode length without the fringing effects of the edges, Figures 2.6 and 2.7.

Large amplitude deflection can be achieved as there is no electrode in the direction of motion in the out of plane direction. Elimination of pull in instability prevents the collapse of the moving plate by stiction to the electrode which is a common problem encountered in device of this kind actuated by parallel plate electrostatic. The lateral pull in of the microbeam is prevented by high lateral stiffness of the moving structure. This large displacement provides a convenient system for experimental and theoretical study structural behavior of this kind of structures without the collapse and stiction.

Figure 2.6: Schematic of a curved microbeam actuated by fringing electrostatic field [41]

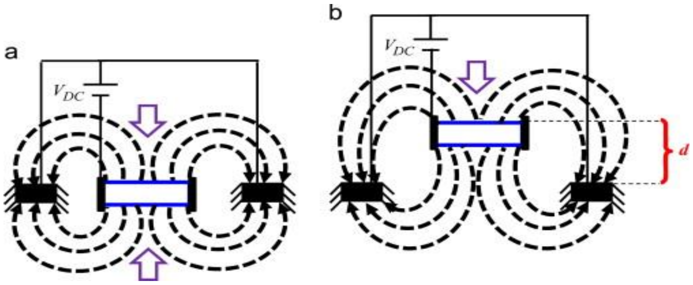

Figure 2.7: Fringing-fields electrostatic actuation method [60].

The analytical expression of this electrostatic force because of the asymmetric fringing fields cannot be obtained explicitly unlike the parallel plate actuation force. Hence numerical approximation of the electrostatic force has to be developed.

Various research groups [38, 41] have suggested various expression through numerical approximation. Krylov et. al. [41] proposed two expressions:

$$\hat{F}_1 = \alpha \frac{\beta \hat{w}}{1+\beta \hat{w}^{2\gamma}} \; ; \; \hat{F}_2 = \alpha \frac{\sinh(\beta \hat{w})}{\cosh^{\gamma}(\beta \hat{w})}, \tag{2.5}$$

where α , β and γ are fitting parameters

Table 2.1 Fitting Parameters [41].

Fitting Functions	α	β	γ
$\hat{F}_1$	4.44×10^{-6}	0.45	1.2
$\hat{F}_2$	2.15×10^{-6}	1.05	1.4

2.4 Symmetric and Asymmetric Bifurcations

Bi-stability is one of curved structure's interesting features which makes its structural behavior rich and interesting for several MEMS applications. Bi-stability refers to presence of two different stable positions for the same applied load. In this case when the applied load is increased, the initially curved beam starts to deflect reducing consequently its elevation. A curved beam with initial mid-point elevation above a certain critical value and at a certain applied load shifts to another stable configuration at a remote location. This phenomenon is well known as snap-through instability motion. Contrary to this when the applied load is decreased the beam exhibits displacements in its post-buckled position until reaching a certain value when the beam shifts back to its pre-buckled position causing a snap-back motion. The snap-through and snap-back loading values are generally not equal displaying the hysteretic nature of the curved beam’s structural behavior. The beam is bi-stable between the two critical instability (snap-through and snap-back) values. The stable branches of the solution are known as nodes and the unstable branch between them is called saddle. At the limit points (snap-through and snap-back) the saddle and node annihilate each other causing a saddle-node bifurcation. When the initial midpoint elevation of the curved microbeam is higher than a particular value, it buckles non-symmetrically causing symmetry breaking of the microbeam. Curved microbeams undergoing symmetry breaking bifurcates at a lower voltage than predicted by the symmetric model [54, 55]. Figure 2.8 shows symmetric and asymmetric bifurcation of a microbeam.

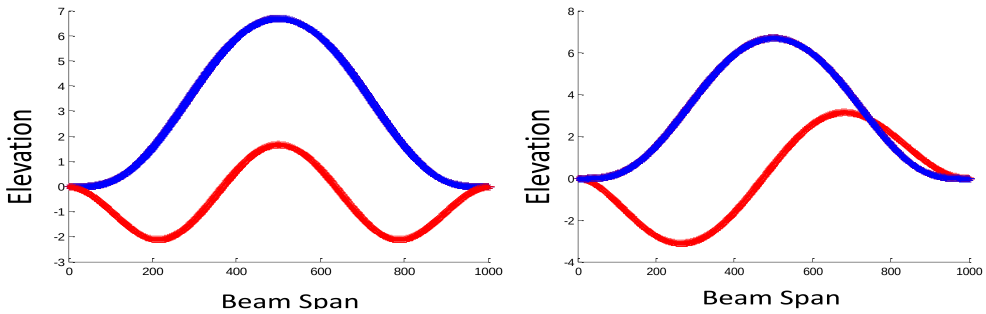

(a) (b)

Figure 2.8: Symmetric (a) and asymmetric (b) bifurcations.

CHAPTER 3

MODELING

In this chapter we derive the equation of motion of a shallow arch actuated with a uniform mechanical load. After that we discuss about the system equations of curved microbeam actuators with parallel plates as well as fringing fields electrostatic loading. A reduced order model (ROM) discretization technique using Galerkin decomposition is used to solve the beam equations.

3.1 The Equation of Motion of a Shallow Arch under Uniform Load

The equation of motion of an initially curved (arch) beam shown in figure 3.1 and its corresponding boundary conditions are derived using the Hamilton's principle. Euler-Bernoulli beam theory is considered to model the beam where we assume that its cross-sectional planes remain parallel even after deformation. We consider a clamped-clamped shallow arch of initial shape $\hat{w}_0\left(\hat{x}\right)$, length L, width b, thickness d, modulus of elasticity E, cross sectional area $A = bd$ and moment of inertia $I = \frac{bh^3}{12}$. We also assume that the beam has mass density ρ and moment of inertia I and it's subjected to a constant axial force of magnitude N as shown in figure 3.1. Let $\hat{w}(\hat{x},\hat{t})$ be the transverse displacement of the beam from its initial position $\hat{w}_0(\hat{x})$ and $\hat{u}(\hat{x},\hat{t})$ represents its axial displacement.

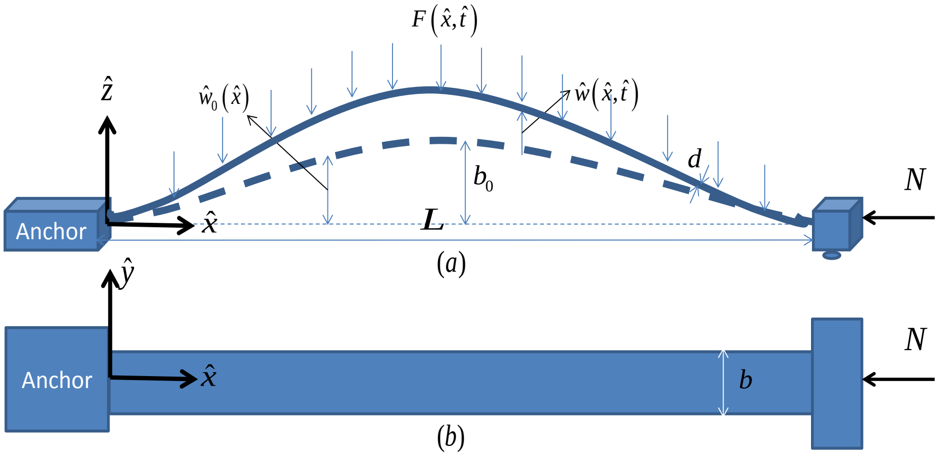

Figure 3.1: (a) Side and (b) top view of a clamped-clamped arch under compressive axial load.

Let A^i be the initial position of point on the beam with x^i coordinate in the axial direction and z^i be the transverse coordinate in figure 3.2. The final position of the point after deformation is A^f with coordinates x^f and z^f. Let us consider a differential element of length dx^i at point A^i. The point is displaced a distance $\hat{u}$ and $\hat{w}$ in the axial and transverse direction respectively. The element getting deformed to dx^f and dz^f axially and transversely.

$$\begin{aligned} x^f &= x^i + \hat{u} = \hat{x} + \hat{u} \\ z^f &= z^i + \hat{w} = \hat{w}_0 + \hat{w} \end{aligned} \tag{3.1}$$

$$d\hat{s}=\sqrt{\left(dx^{f}\right)^{2}+\left(dz^{f}\right)^{2}}=\sqrt{\left(d\hat{x}+d\hat{u}\right)^{2}+\left(d\hat{w}+d\hat{w}_{0}\right)^{2}}=\sqrt{\left(1+\hat{u}'\right)^{2}+\left(\hat{w}'+\hat{w}_{0}'\right)^{2}}\,d\hat{x}, \qquad (3.2)$$

where “ ' ” denotes the first derivative with respect to x .

Expanding the equation (3.2) we get:

$$d\hat{s}=\sqrt{1+2\hat{u}'+\hat{u}'^{2}+\hat{w}'^{2}+2\hat{w}'\hat{w}_{0}'}\,d\hat{x} \qquad (3.3)$$

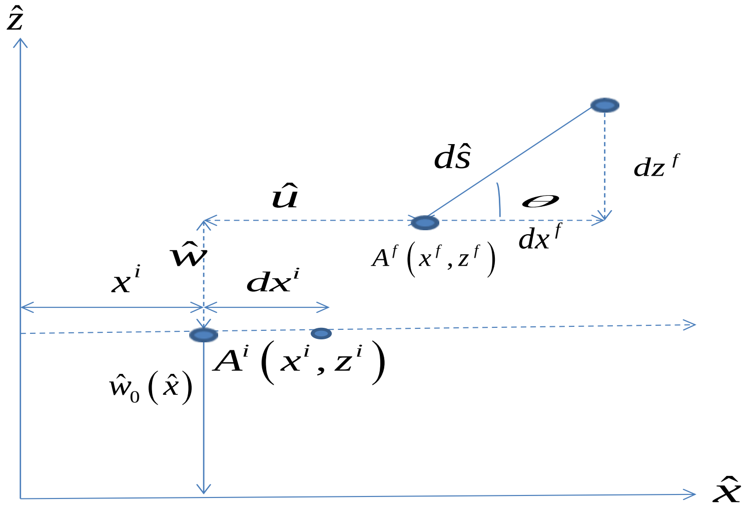

Figure 3.2: Deformation of a beam segment [58].

Considering the approximation for shallow arch where the initial rise slope is small compared to unity $\left(w_{0}'\right)^{2}<<1$ [61], the deformed element strain becomes:

$$\varepsilon=\frac{d\hat{s}-d\hat{x}}{d\hat{x}}=\sqrt{1+2\hat{u}'+\hat{u}'^{2}+\hat{w}'^{2}+2\hat{w}'\hat{w}_{0}'}-1 \qquad (3.4)$$

The beam element stretch ratio is given by:

$$\lambda=\frac{d\hat{s}}{d\hat{x}}=\sqrt{1+2\hat{u}'+\hat{u}'^{2}+\hat{w}'^{2}+2\hat{w}'\hat{w}_{0}'} \qquad (3.5)$$

The angle of rotation in Figure 3.2 is given by:

$$\begin{cases} \sin\theta = \dfrac{dz^{f}}{d\hat{s}} = \dfrac{\hat{w}'_0 + \hat{w}'}{\lambda}, \\ \cos\theta = \dfrac{dx^{f}}{d\hat{s}} = \dfrac{1+\hat{u}'}{\lambda}, \end{cases} \tag{3.6}$$

Differentiating Equation (3.6), we get:

$$\theta' = \frac{\left(1+\hat{u}'\right)\left(\hat{w}''_0 + \hat{w}''\right) - \hat{u}''\left(\hat{w}'_0 + \hat{w}'\right)}{\lambda^2}, \tag{3.7}$$

The midplane curvature of the curved beam is given by

$$k = \frac{d\theta}{d\hat{s}} = \frac{d\theta}{d\hat{x}}\frac{d\hat{x}}{d\hat{s}} = \frac{\left(1+\hat{u}'\right)\left(\hat{w}''_0 + \hat{w}''\right) - \hat{u}''\left(\hat{w}'_0 + \hat{w}'\right)}{\lambda^{3/2}} = \frac{\left(1+\hat{u}'\right)\left(\hat{w}''_0 + \hat{w}''\right) - \hat{u}''\left(\hat{w}'_0 + \hat{w}'\right)}{\left(1+2\hat{u}' + \hat{u}'^2 + \hat{w}'^2 + 2\hat{w}'\hat{w}'_0\right)^{3/2}}, \tag{3.8}$$

Using Taylor Series expansion to Equation (3.4) assuming only quadratic terms for small u' and w' we get:

$$\varepsilon \approx \hat{u}' + \frac{\hat{w}'}{2} + \hat{w}'\hat{w}'_{\mathbf{0}} + \cdots \tag{3.9}$$

The total beam axial strain at a distance z from midplane line of the beam is given by:

$$\varepsilon_T \approx \varepsilon - \hat{z}\hat{w}'' + \cdots \tag{3 .10}$$

Finally the midplane beam curvature given by Equation (3.8) can be simplified by using Taylor series expansion for small u' and w' assuming only quadratic terms:

$$k \approx \left(\hat{w}''_0 + \hat{w}''\right) - \hat{u}''\left(\hat{w}'_0 + \hat{w}'\right) - 2\left(\hat{w}''_0 + \hat{w}''\right)\hat{u}'' + \cdots \tag{3.11}$$

3.1.1 The Potential Energy

The potential energy of the beam due to its midplane stretching and its elastic deformation is given by:

$$V=\frac{1}{2}\int_{0}^{L}\int_{-d/2}^{d/2}\int_{-b/2}^{b/2}\left(E\varepsilon_T^2\right)d\hat{y}d\hat{z}d\hat{x}, \qquad\qquad\qquad \hat{z}^2\Big|_{-d/2}^{d/2}$$

$$=\frac{1}{2}\int_{0}^{L}\int_{-d/2}^{d/2}\int_{-b/2}^{b/2}\left(E\left\{\left(\hat{u}'+\frac{\hat{w}'}{2}+\hat{w}'\hat{w}_0'\right)^2+-\hat{z}\hat{w}''\overset{\nearrow}{\cancel{\left(\hat{u}'+\frac{\hat{w}'}{2}+\hat{w}'\hat{w}'\right)}}^{=0}+\hat{z}^2\hat{w}''^2\right\}\right)d\hat{y}d\hat{z}d\hat{x}, \quad (3.12)$$

$$=\frac{EA}{2}\int_{0}^{L}\left(\hat{u}'+\frac{\hat{w}'}{2}+\hat{w}'\hat{w}'\right)^2d\hat{x}+\frac{EI}{2}\int_{0}^{L}\hat{w}''^2d\hat{x}$$

3.1.2 The Kinetic Energy

The beam's kinetic energy ignoring the axial strain [62] is:

$$T=\frac{\rho A}{2}\int_{0}^{l}\dot{\hat{w}}^2d\hat{x}, \qquad (3.13)$$

where dot is partial derivative with time $\hat{t}$.

3.1.3 The Hamilton Principle

The Hamilton Principle [63, 64] is a useful method to obtain the equation of motion of continuous systems and its boundary condition. It states that for a particular period of time for a conservative mechanical system the integral of the Lagrangian (difference between the Kinetic and the Potential energy) of the system is stationary. The principle can be extended to non-conservative systems in the following manner:

$$\int_{t_1}^{t_2} \partial L d\hat{t} = \int_{t_1}^{t_2} \left(\partial T - \partial V + \partial W_e \right) d\hat{t} = 0, \tag{3.14}$$

where W_e non-conservative work done by external load, V is the elastic potential energy, T kinetic energy and L is the Lagrangian of the system. t_1, t_2 are the initial value and final value of time respectively.

Integrating by parts over time Equation (3.12), the potential energy variation:

$$\int_{t_1}^{t_2} \partial V d\hat{t} = \int_{t_1}^{t_2} \left\{ \begin{array}{l} EA\left[\left(\hat{u}' + \dfrac{\hat{w}'}{2} + \hat{w}'\hat{w}_0' \right) \partial \hat{u} \right]_0^L - EA\displaystyle\int_0^L \left(\hat{u}' + \dfrac{\hat{w}'}{2} + \hat{w}'\hat{w}_0' \right)' \partial \hat{u} d\hat{x} \\ +EA\left[\left(\hat{u}' + \dfrac{\hat{w}'}{2} + \hat{w}'\hat{w}_0' \right) \hat{w}' \partial \hat{w} \right]_0^L - EA\displaystyle\int_0^L \left(\left(\hat{u}' + \dfrac{\hat{w}'}{2} + \hat{w}'\hat{w}' \right) \hat{w}' \right)' \partial \hat{w} d\hat{x} \\ +EA\left[\left(\hat{u}' + \dfrac{\hat{w}'}{2} + \hat{w}'\hat{w}' \right) \hat{w}_0' \partial \hat{w} \right]_0^L - EA\displaystyle\int_0^L \left(\left(\hat{u}' + \dfrac{\hat{w}'}{2} + \hat{w}'\hat{w}_0' \right) \hat{w}_0' \right)' \partial \hat{w} d\hat{x} \\ +EI\left[\hat{w}'' \partial \hat{w}' \right]_0^L - EI\left[\hat{w}''' \partial \hat{w} \right]_0^L + EI\displaystyle\int_0^L \hat{w}'''' \partial \hat{w} d\hat{x} \end{array} \right\} d\hat{t}, \tag{3.15}$$

Integrating by parts over time Equation (2.13), the kinetic energy variation:

$$\begin{aligned} \int_{t_1}^{t_2} \partial T d\hat{t} &= \frac{\rho A}{2} \int_{t_1}^{t_2} \partial \left[\int_0^L \left(\frac{\delta \hat{w}}{\delta t} \right)^2 d\hat{x} \right] d\hat{t} = \rho A \int_0^L \int_{t_1}^{t_2} \left[\frac{\delta \hat{w}}{\delta t} \left(\frac{\delta}{\delta t} \partial \hat{w} \right) \right] d\hat{t} d\hat{x}, \\ &= \rho A \cancelto{t_1=t_2}{\left[\frac{\delta \hat{w}}{\delta \hat{t}} \partial \hat{w} \right]_{t_1}^{t_2}} - \rho A \int_0^L \frac{\partial^2 \hat{w}}{\partial t^2} \partial \hat{w} d\hat{x} = -\rho A \int_0^L \frac{\partial^2 \hat{w}}{\partial t^2} \partial \hat{w} d\hat{x}, \end{aligned} \tag{3.16}$$

3.1.4 Non-conservative Work

The non-conservative work done variation is:

$$\int_{t_1}^{t_2} \partial W_e d\hat{t} = \int_{t_1}^{t_2} \left(F\left(\hat{x}, \hat{t} \right) \partial \hat{w} - c\hat{w} \right) d\hat{t}, \tag{3.17}$$

where F the transversely directed external applied load and c is the coefficient of viscous damping.

Substituting Equations (3.15-3.17) in the Hamilton Principle, Equation (3.14), and gathering the terms with coefficient “∂u”’ we obtain:

$$\left(u' + \frac{w'}{2} + w'w_0'\right)' = 0\,, \tag{3.18}$$

The elongation of the beam in the axial direction is obtained by integrating Equation (3.18) over the beam length as follows:

$$\hat{u}\left(L,\hat{t}\right) - \hat{u}\left(0,\hat{t}\right) = \left(\hat{u}' + \frac{\hat{w}'}{2} + \hat{w}'\hat{w}_0'\right)L - \int_0^L \left(\hat{u}' + \frac{\hat{w}'}{2} + \hat{w}'\hat{w}_0'\right)d\hat{x}, \tag{3.19}$$

where $u\left(L,\hat{t}\right)$ and $u\left(0,\hat{t}\right)$denotes the axial displacement of the beam ends.

From figure 3.1, at $\hat{x} = 0$ the beam is considered fixed and at $\hat{x} = L$ a compressive load N is assumed, hence:

$$\hat{u}\left(L,\hat{t}\right) = -\frac{NL}{EA}, \tag{3.20}$$

Plugging Equation (3.20) into Equation (3.19), we get:

$$\hat{u}' + \frac{\hat{w}'}{2} + \hat{w}'\hat{w}_0' = -\frac{N}{EA} + \frac{1}{L}\int_0^L \left(\hat{u}' + \frac{\hat{w}'}{2} + \hat{w}'\hat{w}_0'\right)d\hat{x}, \tag{3.21}$$

Gathering the terms with coefficient “∂w” after substituting Equations (3.15-3.17) in the Hamilton Principle Equation (3.14) we get:

$$\rho A\ddot{\hat{w}}+EI\hat{w}''''+c\dot{\hat{w}}=EA\left(\hat{u}'+\frac{\hat{w}'}{2}+\hat{w}'\hat{w}_0'\right)'\left(\hat{w}_0'+\hat{w}'\right)+EA\left(\hat{u}'+\frac{\hat{w}'}{2}+\hat{w}'\hat{w}_0'\right)\left(\hat{w}_0''+\hat{w}''\right)+F\left(\hat{x},\hat{t}\right) \quad (3.22)$$

Hence the nonlinear equation of motion of the shallow arch after substituting Equations (3.18-3.21) into Equation (3.22) we get:

$$\rho A\ddot{\hat{w}}+EI\hat{w}''''+c\dot{\hat{w}}=\left(-N+\frac{EA}{2L}\int_0^L\left(\hat{w}'^2+2\hat{w}'\hat{w}_0'\right)d\hat{x}\right)\left(\hat{w}_0''+\hat{w}''\right)+F\left(\hat{x},\hat{t}\right), \quad (3.23)$$

which represents the equation of the shallow arch for its displacement in the transverse direction from its initial position denoted by $\hat{w}\left(\hat{x}\right)$ in Figure 3.1.

3.2 Parallel-Plates Electrostatic Actuator

3.2.1 Equation of Motion.

We consider here a clamped-clamped curved microbeam of initial shape $\hat{w}_0\left(\hat{x}\right)$ and with same dimension of the microbeam discussed in section 3.1. The initial elevation of the beam midpoint is $\hat{h}$. The arch is actuated by parallel electrode at the bottom of the arch after a gap of g_0.

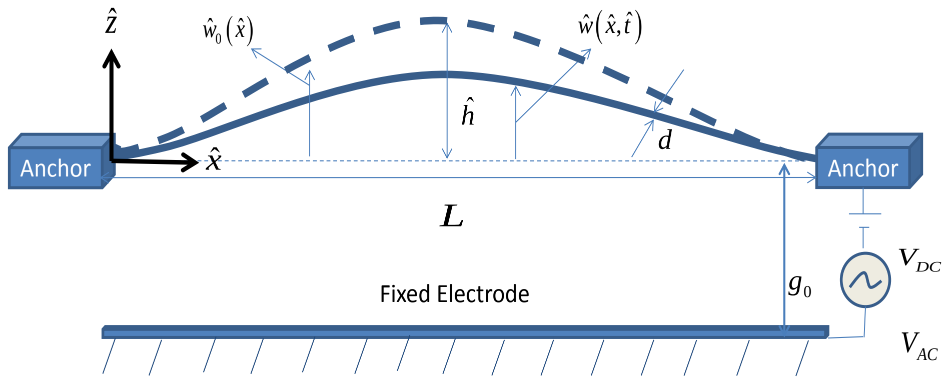

Figure 3.3: Side view of clamped-clamped arch actuated by parallel plate electrode.

The non-linear equation of motion of the arch assuming Euler-Bernoulli beam model for the transverse elevation $\hat{w}\left(\hat{x},\hat{t}\right)$ is

$$EI\frac{\partial^4 \hat{w}}{\partial \hat{x}^4}+\rho A\frac{\partial^2 \hat{w}}{\partial \hat{t}^2}+\hat{c}\frac{\partial \hat{w}}{\partial \hat{t}}=\frac{EA}{2L}\left[\int_0^L\left(\left(\frac{\partial \hat{w}}{\partial \hat{x}}\right)^2-2\frac{\partial \hat{w}}{\partial \hat{x}}\frac{\partial \hat{w}_0}{\partial \hat{x}}\right)d\hat{x}\right]\left[\frac{\partial^2 \hat{w}}{\partial \hat{x}^2}-\frac{d^2 \hat{w}_0}{d\hat{x}^2}\right]+\hat{N}\left[\frac{\partial^2 \hat{w}}{\partial \hat{x}^2}-\frac{d^2 \hat{w}_0}{d\hat{x}^2}\right]+F_e(\hat{x},\hat{t}), \quad (3.24)$$

where the electrostatic actuation force is given by the following analytical expression [1, 28, 65]:

$$F_e(\hat{x},\hat{t})=\frac{\in_0 b\left(V_{DC}+V_{AC}\cos\left(w_f\hat{t}\right)\right)^2}{2\left(g_0+w_0(\hat{x})-\hat{w}(\hat{x},\hat{t})\right)^2}, \quad (3.25)$$

where $\in_0$ is the air dielectric constant.

For convenience, we assume the following non-dimensional parameters to normalize the above equation of motion:

$$w=\frac{\hat{w}}{g_0};\;\; w_0=\frac{\hat{w}_0}{g_0};\;\; h=\frac{\hat{h}}{g_0};\;\; x=\frac{\hat{x}}{L};\;\; t=\frac{\hat{t}}{T}; \quad (3.26)$$

Substituting Equations (3.25) and (3.26) in Equation (3.24), we get:

$$\begin{aligned}&EI\frac{\partial^4\left(g_0\times w\right)}{\partial\left(L\times x\right)^4}+\rho A\frac{\partial^2\left(g_0\times w\right)}{\partial\left(t\times T\right)^2}+\hat{c}\frac{\partial\left(g_0\times w\right)}{\partial\left(t\times T\right)}=\\&\frac{EA}{2L}\left[\int_0^L\left(\left(\frac{\partial\left(g_0\times w\right)}{\partial\left(L\times x\right)}\right)^2-2\frac{\partial\left(g_0\times w\right)}{\partial\left(L\times x\right)}\frac{\partial\left(g_0\times w_0\right)}{\partial\left(L\times x\right)}\right)d\left(L\times x\right)\right]\left[\frac{\partial^2\left(g_0\times w\right)}{\partial\left(L\times x\right)^2}-\frac{d^2\left(g_0\times w_0\right)}{d\left(L\times x\right)^2}\right]\\&+\hat{N}\left[\frac{\partial^2\left(g_0\times w\right)}{\partial\left(L\times x\right)^2}-\frac{d^2\left(g_0\times w_0\right)}{d\left(L\times x\right)^2}\right]+\frac{\in_0 b\left(V_{DC}+V_{AC}\cos\left(w_f\left(t\times T\right)\right)\right)^2}{2\left(g_0+\left(g_0\times w_0\right)-\left(g_0\times w\right)\right)^2},\end{aligned} \quad (3.27)$$

Simplifying Equation (3.27), we get:

$$\frac{EI\times g_0}{L^4}w'''' + \frac{\rho A\times g_0}{T^2}\ddot{w} + \frac{\hat{c}\times g_0}{T}\dot{w} = \frac{EA}{2L}\left[\frac{d^2}{L}\int_0^1\left(\left(w'\right)^2 - 2w'w_0'\right)dx\right]\times\frac{g_0}{L^2}\left[w'' - w_0''\right]$$
$$+\hat{N}\frac{g_0}{L^2}\left[w'' - w_0''\right] + \frac{\in_0 b\left(V_{DC} + V_{AC}\cos\left(\hat{w}_f t\right)\right)^2}{2g_0^{\,2}\left(1 + w_0 - w\right)^2}, \tag{3.28}$$

where ‘dots’ denote derivative with respect to time variable t and ‘primes’ denote derivative with respect to space variable x.

Multiplying Equation (3.28) by $\frac{L^4}{EI\times g_0}$ we get:

$$w'''' + \frac{\rho A\times d}{T^2}\times\frac{L^4}{EI\times g_0}\ddot{w} + \frac{\hat{c}\times g_0}{T}\times\frac{L^4}{EI\times d}\dot{w} = \frac{EA}{2L}\times\frac{g_0^{\,3}}{L^3}\times\frac{L^4}{EI\times g_0}\left[\int_0^1\left(\left(w'\right)^2 - 2w'w_0'\right)dx\right]\left[w'' - w_0''\right]$$
$$+\hat{N}\frac{g_0}{L^2}\times\frac{L^4}{EI\times g_0}\left[w'' - w_0''\right] + \frac{\in_0 b}{2g_0^{\,2}}\times\frac{L^4}{EI\times g_0}\frac{\left(V_{DC} + V_{AC}\cos\left(\hat{w}_f t\right)\right)^2}{\left(1 + w_0 - w\right)^2}, \tag{3.29}$$

Finally simplifying Equation (3.29), we get:

$$w'''' + \ddot{w} + c\dot{w} = \alpha_1\left[\int_0^1\left(\left(w'\right)^2 - 2w'w_0'\right)dx\right]\left[w'' - w_0''\right] + N\left[w'' - w_0''\right] + \alpha_2\frac{\left(V_{DC} + V_{AC}\cos\left(\hat{w}_f t\right)\right)^2}{\left(1 + w_0 - w\right)^2}, \tag{3.30}$$

while considering that $\frac{\rho A L^4}{T^2 EI} = 1$ and $w_0\left(x\right) = \frac{h}{2}\left(1 - \cos\left(2\pi x\right)\right)$, and where the various non-dimensional parameters of equation (3.20) are summarized in the following table:

Table 3.1: Non-Dimensional Parameters for Parallel Plates Actuated Arch.

$c = \frac{\hat{c}L^4}{T \times EI}$	Damping Parameter
$\alpha_1 = \frac{Ag_0^{\ 2}}{2I} = \frac{b \times d \times g_0^{\ 2}}{2 \times \frac{1}{12} b \times d^3} = 6\left(\frac{g_0}{d}\right)^2$	Stretching Parameter
$\alpha_2 = \frac{\in_0 bL^4}{2g_0^{\ 3}EI} = \frac{6 \in_0 L^4}{Eg_0^{\ 3}d^3}$	Electric Force Parameter
$N = \hat{N}\frac{g_0}{L^2} \times \frac{L^4}{EI \times g_0} = \hat{N}\frac{L^2}{EI}$	Axial Force Parameter
$T = \sqrt{\frac{\rho AL^4}{EI}}$	Time Constant
$\omega_f = \frac{\hat{\omega}_f}{T}$	Excitation Frequency Parameter

We let

$$\Gamma = \int_0^1 \left(w'\right)^2 dx;\ \ \Gamma_1 = \int_0^1 \left(w' w_0'\right) dx; \tag{3.31}$$

If we assume zero axial force (N=0), Equation (3.30) reduces to,

$$w'''' + \ddot{w} + c\dot{w} = \alpha_1\left[\Gamma - 2\Gamma_1\right]\left[w'' - w_0''\right] + \alpha_2 \frac{\left(V_{DC} + V_{AC}\cos\left(\hat{w}_f t\right)\right)^2}{\left(1 + w_0 - w\right)^2}, \tag{3.32}$$

and where the corresponding boundary conditions are:

$$w\left(0,t\right) = 0, \frac{\delta w}{\delta x}\left(0,t\right) = 0, w\left(1,t\right) = 0, \frac{\delta w}{\delta x}\left(1,t\right) = 0, \qquad 33)$$

3.2.2 Reduced-Order Model (ROM).

There are several ways in which the beam equation can be solved. We have selected to use here the Galerkin expansion to get a Reduced-Order Model (ROM) ([44, 45]), where the elevation of the shallow arch is approximated as

$$w(x,t)=\sum_{i=1}^{n}u_i(t)\phi_i(x), \tag{3.34}$$

where $\phi_i(x)$ are the trial functions which satisfy the boundary conditions. They are considered to be the linear undamped eigenmodes of the straight unactuated microbeam. $u_i(t)$ are the non-dimensional time varying modal coordinates.

The mode shapes of a clamped-clamped straight beam are given by the following expression:

$$\phi_i(x)=\cosh\beta_i x-\cos\beta_i x+\lambda_i(\sin\beta_i x-\sinh\beta_i x), \tag{3.35}$$

where $\beta_i=\frac{(2i+1)\pi}{2}$, and $\lambda_i=0.9825$, $\lambda_i\approx 1$ for $i\succ 1$.

$\phi_i(x)$ are normalized as follows:

$$\int_0^1\phi_i(x)\phi_j(x)dx=\delta_{ij}=\begin{cases}1\cdots i=j\\0\cdots i\neq j\end{cases}, \tag{3.36}$$

Multiplying the discretized equations with $\phi_i(x)$ and integrating from 0 to 1, we obtain the following differential equation in term of modal coordinates $u_i(t)$

$$\sum_{i=1}^{n}M_{ij}\ddot{u}_i(t)+\sum_{i=1}^{n}C_{ij}\dot{u}_j(t)+\sum_{i=1}^{n}K_{ij}u_j(t)=F_j(t) \tag{3.37}$$

where

$$M_{ij} = \int_0^1 \left[\phi_i(x) \phi_j(x) \right] dx\,;$$

$$C_{ij} = c\int_0^1 \left[\phi_i(x) \phi_j(x) \right] dx\,;$$

$$K_{ij} = \int_0^1 \left[\phi_i''''(x) \phi_j(x) \right] dx; \tag{3.38}$$

$$F_j(t) = \alpha_1 \Gamma \left\{ \int_0^1 \left(\sum_{i=1}^{n} u_i(t) \phi_i' \right)^2 dx + 2\int_0^1 \left(\sum_{i=1}^{n} u_i(t) \phi_i' \frac{dw_0}{dx} \right) dx \right\} +$$
$$+ \alpha_2 \frac{\left(V_{DC} + V_{AC} \cos(\Omega t) \right)^2}{\left(1 + w_0 + \sum_{i=1}^{n} u_i(t) \phi_i(x) \right)} \int_0^1 \phi_j(x)\, dx$$

$$\forall i, j = 1..n.$$

and where

$$\Gamma = \int_0^1 \left\{ \phi_j(x) \left(\sum_{i=1}^{n} u_i \phi_i''(x) \right) - \frac{d^2 w_0}{dx^2} \right\} dx \tag{3.39}$$

3.3 Fringing Fields Electrostatic Actuator Curved Microbeams

3.3.1 Equation of Motion.

We consider here the same clamped-clamped curved microbeam of Section 3.2 while actuated by fringing fields electric force. Two ground electrodes are placed on both sides of the curved beam in the same plane as the ends of the microbeam. Due to curvature of the beam there is asymmetric distribution of electric field which produces net electrostatic force acting on the beam towards the plane of the electrodes.

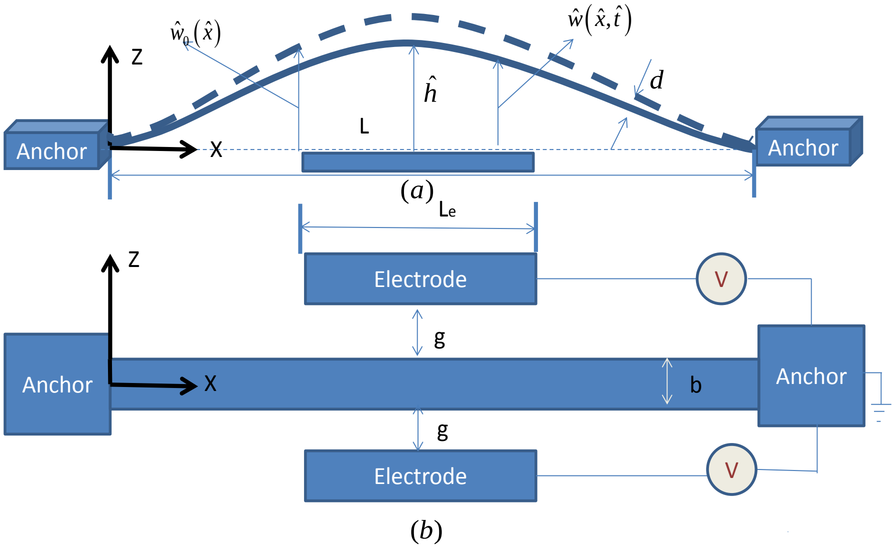

Figure 3.4: (a) Side and (b) top views of a clamped-clamped arch actuated by fringing fields electrostatic force.

The non-linear equation of motion of the arch assuming Euler-Bernoulli beam model for the transverse elevation $\hat{w}(\hat{x},\hat{t})$ is:

$$EI\frac{\partial^4\hat{w}}{\partial\hat{x}^4}+\rho A\frac{\partial^2\hat{w}}{\partial\hat{t}^2}+\hat{c}\frac{\partial\hat{w}}{\partial\hat{t}}=\frac{EA}{2L}\left[\int_0^L\left(\left(\frac{\partial\hat{w}}{\partial\hat{x}}\right)^2-2\frac{\partial\hat{w}}{\partial\hat{x}}\frac{\partial\hat{w}_0}{\partial\hat{x}}\right)d\hat{x}\right]\left[\frac{\partial^2\hat{w}}{\partial\hat{x}^2}-\frac{d^2\hat{w}_0}{d\hat{x}^2}\right]+\hat{N}\left[\frac{\partial^2\hat{w}}{\partial\hat{x}^2}-\frac{d^2\hat{w}_0}{d\hat{x}^2}\right]+F_e(\hat{x},\hat{t}),\quad(3.40)$$

where the fringing fields electrostatic force is given by the following fitting expression [41]:

$$F_e(\hat{x},\hat{t})=\frac{a\sinh\left(\sigma\left(w_0-w\right)\right)V^2}{\cosh^p\left(\sigma\left(w_0-w\right)\right)}H\left(\hat{x}-\frac{L-\hat{L}_e}{2L}\right)H\left(\hat{L}_e+\frac{L-\hat{L}_e}{2L}-\hat{x}\right),\qquad(3.\ 41)$$

For convenience, we assume the following non-dimensional parameters to normalize the above equation of motion:

$$w=\frac{\hat{w}}{d};\quad w_0=\frac{\hat{w}_0}{d};\quad h=\frac{\hat{h}}{d};\quad x=\frac{\hat{x}}{L};\quad t=\frac{\hat{t}}{T};\ L_e=\frac{\hat{L}_e}{L};\qquad(3.42)$$

Substituting Equations (3.41) and (3.42) into Equation (3.40), we get:

$$\begin{gathered}EI\frac{\partial^4\left(d\times w\right)}{\partial\left(L\times x\right)^4}+\rho A\frac{\partial^2\left(d\times w\right)}{\partial\left(t\times T\right)^2}+\hat{c}\frac{\partial\left(d\times w\right)}{\partial\left(t\times T\right)}=\\ \frac{EA}{2L}\left[\int_0^L\left(\left(\frac{\partial\left(d\times w\right)}{\partial\left(L\times x\right)}\right)^2-2\frac{\partial\left(d\times w\right)}{\partial\left(L\times x\right)}\frac{\partial\left(d\times w_0\right)}{\partial\left(L\times x\right)}\right)d\left(L\times x\right)\right]\left[\frac{\partial^2\left(d\times w\right)}{\partial\left(L\times x\right)^2}-\frac{d^2\left(d\times w_0\right)}{d\left(L\times x\right)^2}\right]\\ +\hat{N}\left[\frac{\partial^2\left(d\times w\right)}{\partial\left(L\times x\right)^2}-\frac{d^2\left(d\times w_0\right)}{d\left(L\times x\right)^2}\right]+\frac{a\sinh\left(\sigma\left(w_0-w\right)\right)V^2}{\cosh^p\left(\sigma\left(w_0-w\right)\right)}H\left(x-\frac{1-L_e}{2}\right)H\left(L_e+\frac{1-L_e}{2}-x\right)=0\end{gathered}\tag{3.43}$$

Simplifying Equation (3.43), we get:

$$\begin{gathered}\frac{EI\times d}{L^4}w^{''''}+\frac{\rho A\times d}{T^2}\ddot{w}+\frac{\hat{c}\times d}{T}\dot{w}=\frac{EA}{2L}\left[\frac{d^2}{L}\int_0^1\left(\left(w'\right)^2-2w'w_0'\right)dx\right]\times\frac{d}{L^2}\left[w''-w_0''\right]\\ +\hat{N}\frac{d}{L^2}\left[w''-w_0''\right]+\frac{a\sinh\left(\sigma\left(w_0-w\right)\right)V^2}{\cosh^p\left(\sigma\left(w_0-w\right)\right)}H\left(x-\frac{1-L_e}{2}\right)H\left(L_e+\frac{1-L_e}{2}-x\right)=0\end{gathered}\tag{3.44}$$

Multiplying Equation (3.44) with $\frac{L^4}{EI\times\hat{d}}$, we get:

$$\begin{gathered}w''''+\frac{\rho A\times d}{T^2}\times\frac{L^4}{EI\times\hat{d}}\ddot{w}+\frac{\hat{c}\times d}{T}\times\frac{L^4}{EI\times d}\dot{w}=\frac{EA}{2L}\times\frac{d^3}{L^3}\times\frac{L^4}{EI\times d}\left[\int_0^1\left(\left(w'\right)^2-2w'w_0'\right)dx\right]\left[w''-w_0''\right]\\ +\hat{N}\frac{d}{L^2}\times\frac{L^4}{EI\times d}\left[w''-w_0''\right]+\frac{L^4}{EI\times d}\times\frac{a\sinh\left(\sigma\left(w_0-w\right)\right)V^2}{\cosh^p\left(\sigma\left(w_0-w\right)\right)}H\left(x-\frac{1-L_e}{2}\right)H\left(L_e+\frac{1-L_e}{2}-x\right)\end{gathered}\tag{3.45}$$

Simplifying Equation (3.45)

$$\begin{gathered}w''''+\ddot{w}+c\dot{w}=\alpha_1\left[\int_0^1\left(\left(w'\right)^2-2w'w_0'\right)dx\right]\left[w''-w_0''\right]+N\left[w''-w_0''\right]+\\ +\alpha_2V^2\frac{\sinh\left(\sigma\left(w_0-w\right)\right)}{\cosh^p\left(\sigma\left(w_0-w\right)\right)}H\left(x-\frac{1-L_e}{2}\right)H\left(L_e+\frac{1-L_e}{2}-x\right)\end{gathered}\tag{3.46}$$

while considering that $\frac{\rho AL^4}{T^2 EI}=1$ and $w_0\left(x\right)=\frac{h}{2}\left(1-\cos\left(2\pi x\right)\right)$ with Γ and Γ_1 are same as in equation (3.31) with the various non-dimensional parameters same with table 3.1 with only the following difference :

Table 3.2: Non-Dimensional Parameters for Fringing Fields Actuated Arch.

$\alpha_1=\frac{Ad^2}{2I}=\frac{b\times d\times d^2}{2\times\frac{1}{12}b\times d^3}=6$	Stretching Parameter
$\alpha_2=\frac{aV^2L^4}{EI\times d}$	Electric Force Parameter

If there is no axial force N=0 the Equation (3.46) now reduces to,

$$w'''' + \ddot{w} + c\dot{w} = \alpha_1\left[\Gamma - 2\Gamma_1\right]\left[w'' - w_0''\right] + \alpha_2 V^2 \frac{\sinh\left(\sigma\left(w_0 - w\right)\right)}{\cosh^p\left(\sigma\left(w_0 - w\right)\right)} H\left(x - \frac{1-0.25}{2}\right) H\left(0.25 + \frac{1-0.25}{2} - x\right), \quad (3.47)$$

The corresponding boundary conditions for the clamped-clamped beam are same as Equation (3.33).

3.3.2 Reduced-Order Model (ROM).

We have used here the Galerkin decomposition as a discretization technique to obtain the Reduced-Order Model (ROM) similarly as it was applied to curved beams with parallel plate actuation in section 3.2.2. Similarly multiplying the discretized equation with $\phi_i\left(x\right)$ and integrating from 0 to 1 to obtain the following differential equation in term of modal coordinate's $u_i\left(t\right)$ same as the equation (3.37), with M_{ij}, C_{ij} and K_{ij} as in equation (3.38) and with the following different $F_j\left(t\right)$:

$$
\begin{aligned}
F_j\left(t\right)=\alpha_1\Gamma\left\{\int_0^1\left(\sum_{i=1}^{n}u_i\left(t\right)\phi_i'\right)^2 dx+2\int_0^1\left(\sum_{i=1}^{n}u_i\left(t\right)\phi_i'\,\frac{dw_0}{dx}\right)dx\right\}+\\
+\alpha_2\frac{a\sinh\left(\sigma\left(w_0-\sum_{i=1}^{n}u_i\left(t\right)\phi_i\left(x\right)\right)\right)V^2}{\cosh^p\left(\sigma\left(w_0-\sum_{i=1}^{n}u_i\left(t\right)\phi_i\left(x\right)\right)\right)}H\left(x-\frac{1-0.25}{2}\right)H\left(0.25+\frac{1-0.25}{2}-x\right)\int_0^1\phi_j\left(x\right)dx
\end{aligned}
\tag{3.48}
$$

$$\forall i,\, j=1..n.$$

where Γ is given by equation (3.39).

CHAPTER 4

STATIC ANALYSIS

In this chapter we carry out the static analysis of MEMS arch actuated by parallel plates as well as by fringing fields electrostatic force. Result for the static analysis for the parallel plate actuation is compared with relevant literature to show the validation of our model. Arches with various initial midpoint elevations are considered.

4.1 Static Response Considering Parallel Plates Electrostatically Actuated MEMS Arch

We consider a clamped-clamped shallow MEMS arch with the geometrical and material parameters summarized in the following table:

Table 4.1: case study parameters for parallel plates actuation.

Length	$L = 1000\mu m$
Width	$b = 30\mu m$
Thickness	$d = 2.4\mu m$
Electrode Gap	$g_0 = 10.1\mu m$
Density	$\rho = 2332 Kg / m^3$
Young's Modulus	$\hat{E} = 154 GPa$
Poisson's Ratio	$\nu = 0.27$

Assuming a plain-strain theory and knowing that the beam's width is greater than its thickness, the effective Young's modulus for the investigated beam can be expressed as $E = \hat{E}/\left(1-\nu^2\right) = 169GPa$.

The above case study is selected to be able to compare the numerical results with the one already been published (Krylov et al. [1] and Ouakad and Younis [29]). Ouakad and Younis [29] showed that the contribution of the anti-symmetric modes in ROM for these type of arches is negligible. Hence only symmetric modes are considered in the ROM analysis. Convergence of the number of modes for the ROM is studied to find out the minimum number of modes required to get accurate result. Figure 4.1 presents the deflection of the midpoint of the arch for various numbers of modes. It shows the absolute deflection of the midpoint of the arch. We can clearly see that using five modes provides sufficiently converged results. Snap through occurs at about $V_{DC} = 88$ Volt and pull-in voltage was found to be $V_{DC} = 106$ Volts which agrees with the results of [21].

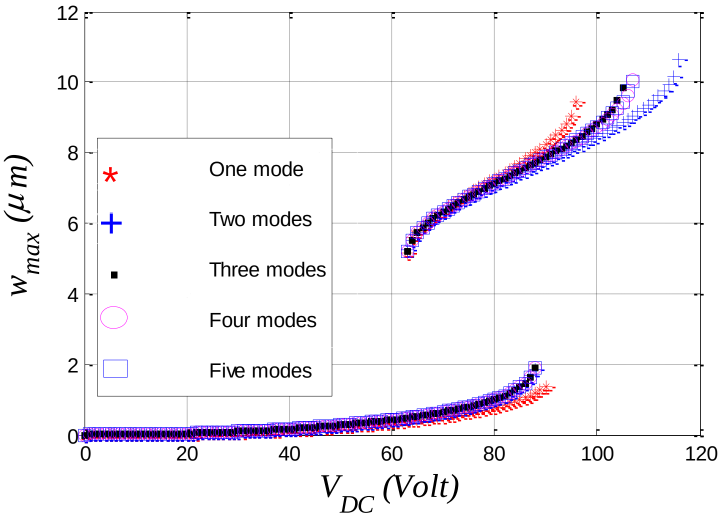

Figure 4.1: Midpoint static deflection of shallow arch with the DC voltage for various number of symmetric mode shapes of a straight beam in the ROM

4.2 Static Response Considering Fringing Field Electrostatically Actuated MEMS Arch

We consider now in this Section a clamped-clamped arch with two electrodes located at both sides of the beam shown in the figure 3.4. The electrodes are kept smaller than the beam to have an approximately equal distribution of electrostatic force throughout the beam and to get rid of the fringing effect of the beam's end. The lengths of the electrodes are one-fourth of the beam in this case. The beam is made up of polysilicon whose geometrical and material properties are summarized in Table 4.2.

Table 4.2: case study parameters for fringing fields actuation.

Length	$L = 1000 \mu m$
Width	$b = 16 \mu m$
Thickness	$d = 3 \mu m$
Distance to Electrode	$g = 3 \mu m$
Ratio of the length of each electrode to the length of the beam	$L_e = 0.25$
Density	$\rho = 2332 Kg / m^3$
Young's Modulus	$\hat{E} = 154 GPa$
Poisson's Ratio	$\nu = 0.27$

4.2.1 Static Analysis for Initial Midpoint Elevation $\hat{h} = 4.5\mu m$:

The ROM results of figure 4.2 shows the midpoint maximum elevation at various voltages for the case of $\hat{h} = 4.5\mu m$ initial elevation of the beam. The one mode and two modes ROM are almost on top of each other. This presents the convergence of the static equation of the ROM model and suggests that using one mode yields acceptable results. The figure 4.2 shows also good agreement between ROM model and the model of Krylov et al. [41] which uses displacement control approach [66] using Matlab package to solve the ROM nonlinear equations. We can clearly see from the same figure that there is no snap through motion of the beam and it has a stable mode of operations for the entire range of loading suppressing the bi-stability. Snap through motion is observed for the same initial $\hat{h}$ when the actuation is either parallel plate electrode [1, 29] or only mechanical loading [1]. There is a linear region for a small range of voltage (approximately from 120 V to 140 V) in the figure where the slope of the elevation curve is constant. For higher DC load, the beam settles at an almost straight position and does not deflect below to the other side. The downward force is equal to the upward force which results in a zero net force. The net force remains zero even with further increase in the DC voltage. Hence the beam settles down at the straight position and is not deflected downwards with further increase in the DC voltage. This phenomenon is contrary to the conventional parallel plate actuation where there is occurrence of snap-through followed by pull-in where the beam sticks to the lower parallel electrode.

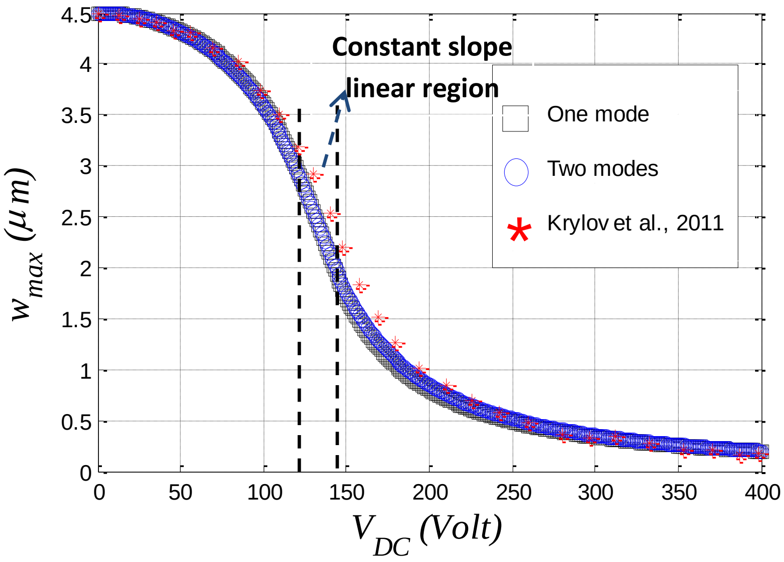

Figure 4.2: Variation of midpoint static elevation for $\hat{h} = 4.5\mu m$ with DC voltage for various symmetric mode shapes and its comparison with the results of Krylov et al. [41].

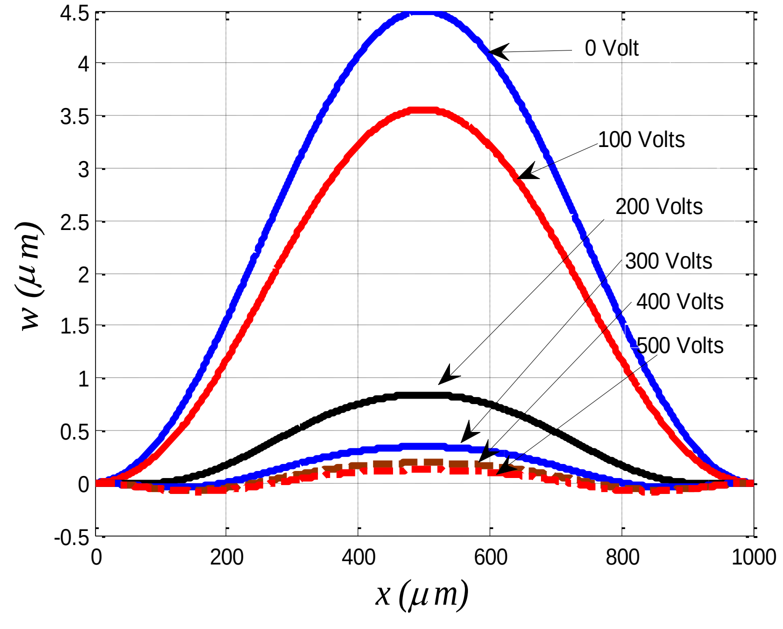

Figure 4.3: The beam static profile for various DC voltages and for the case of $\hat{h} = 4.5\mu m$.

We can explain this behavior by plotting the static profile of the beam for various DC loads as depicted in figure 4.3. The figure shows that initially as the DC voltage is increased the beam deflects downwards. For higher DC voltages, the beam becomes almost straight without any further static deflection even with increase in the applied DC load.

4.2.2 Static Analysis for Initial Midpoint Elevation $\hat{h} = 9\mu m$:

When the beam initial midpoint elevation is increased higher sufficiently we start to observe a change in its static behavior. Higher initial elevation satisfying the conditions of bifurcations causing the arch to jump from one position to another will cause irrigation of its bi-stable behavior. This transition between the bifurcation branches occurs with an asymmetric trend in this case making the microbeam undergoing symmetry breaking along its length. To further demonstrate this figure 4.4 shows the variation of the midpoint elevation of curved microbeam with $\hat{h} = 9\mu m$ elevation and varying the applied DC load. It is worth to note that there is a need to take into account the anti-symmetric mode shapes in this case to get the correct picture of the symmetric breaking unlike the previously investigated cases. The beam in this case observes an asymmetric shape. Hence the net electrostatic force is not reaching zero like what happened in the case of $\hat{h} = 4.5\mu m$. Therefore with sufficient increase in the DC load the beam regains its symmetry to reach zero electrostatic net force. It is worth to mention that the microbeam does not become perfectly straight but undertakes a shape close to the third mode shape of beam. These transitions become clearer when we plot the static profile of the arch for the initial midpoint elevation of $\hat{h} = 9\mu m$, figure 4.5. It shows the loss and regain symmetry of the microbeam with the increase in the DC applied voltage.

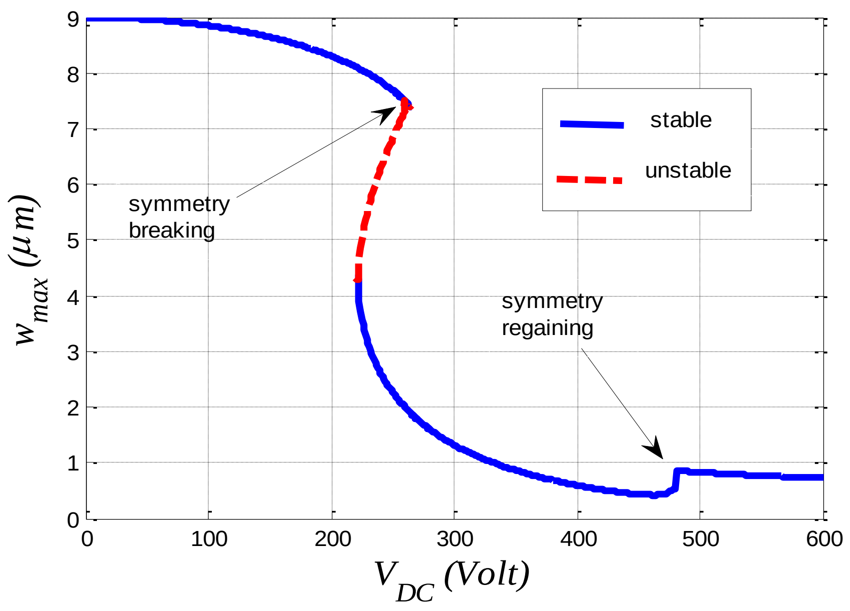

Figure 4.4: Variation of midpoint static elevation for $\hat{h} = 9\mu m$ with DC voltage.

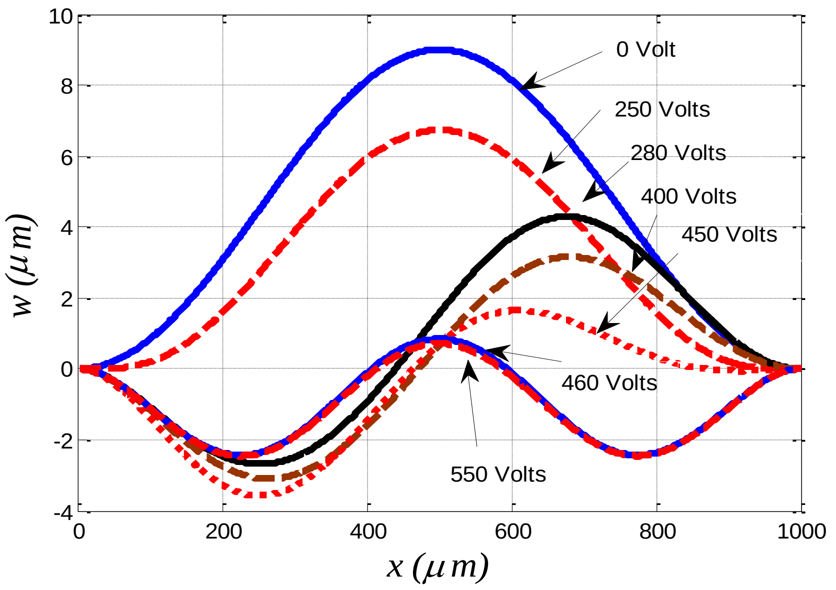

Figure 4.5: The static profile for various DC voltages for $\hat{h} = 9\mu m$.

CHAPTER 5

EIGENVALUE PROBLEM

In this Chapter, we discuss the derivation the natural frequencies and mode shapes from the ROM equation of the MEMS arch. We consider the case the cases of parallel plates as well as fringing field electrostatic actuation. Various cases of initial elevations were considered for the fringing field actuation to see the effect of elevation on natural frequencies.

5.1 Natural Frequencies and Mode Shapes

The variation of the natural frequencies and mode shapes with the applied DC load are investigated in this chapter. The ROM system of equations of the investigated microbeam can be written in the following matrix form:

$$M\left(u\right)\dot{u}=R\left(u\right), \tag{5.1}$$

where

$$u=\left[u_1,u_2,u_3,...,u_n\right], \tag{5.2}$$

is the modal coordinate vector, $M\left(u\right)$ Coefficient of $\dot{u}$ and $R\left(u\right)$ is the right hand side forcing, stiffness and damping coefficients vector. $M\left(u\right)$ and $R\left(u\right)$ are nonlinear functions of modal coordinates $u_i\left(t\right)$ [29].

Splitting the modal coordinate into a static component and a dynamic component

$$u = X_s + \eta(t), \tag{5.3}$$

where X_s is the static equilibrium position under a DC load and $\eta(t)$ is an assumed dynamic perturbation around the equilibrium state.

Plugging Equation 5.3 into Equation 5.1 and expanding using Taylor series. While keeping only the linear terms of $\eta(t)$ and eliminating the higher order term, we obtain a linear function of $\eta(t)$, such as:

$$M(X_s)\dot{\eta} = J(X_s)\eta, \tag{5.4}$$

where $J(X_s)$ is the Jacobian matrix of equilibrium point.

The natural frequency for a particular given voltage can be obtained by substituting the static solution X_s discussed in chapter 4 at that particular voltage to the $M^{-1}J$ matrix and calculating the eigenvalues. Mathematica® software was used to obtain the eigenvalues for the corresponding voltages using 'Eigenvalues' function. The square root of each eigenvalues will give the natural frequencies at a certain voltage. The mode shapes can be obtained by getting the Eigen functions for each eigenvalue using 'Eigenfunctions' in Mathematica®.

The total number of natural frequencies that can be obtained depends on the number of assumed modes in ROM system. A given number of modes will result in $M^{-1}J$ square matrix of the same order. Hence the number of eigenvalues obtained will be same as the number of mode considered.

5.2 Considering Parallel Plates Electrostatic MEMS Arch Actuator:

We consider in this Section the clamped-clamped arch actuated by parallel plate electrostatic force with the parameters mentioned in Table 4.1.

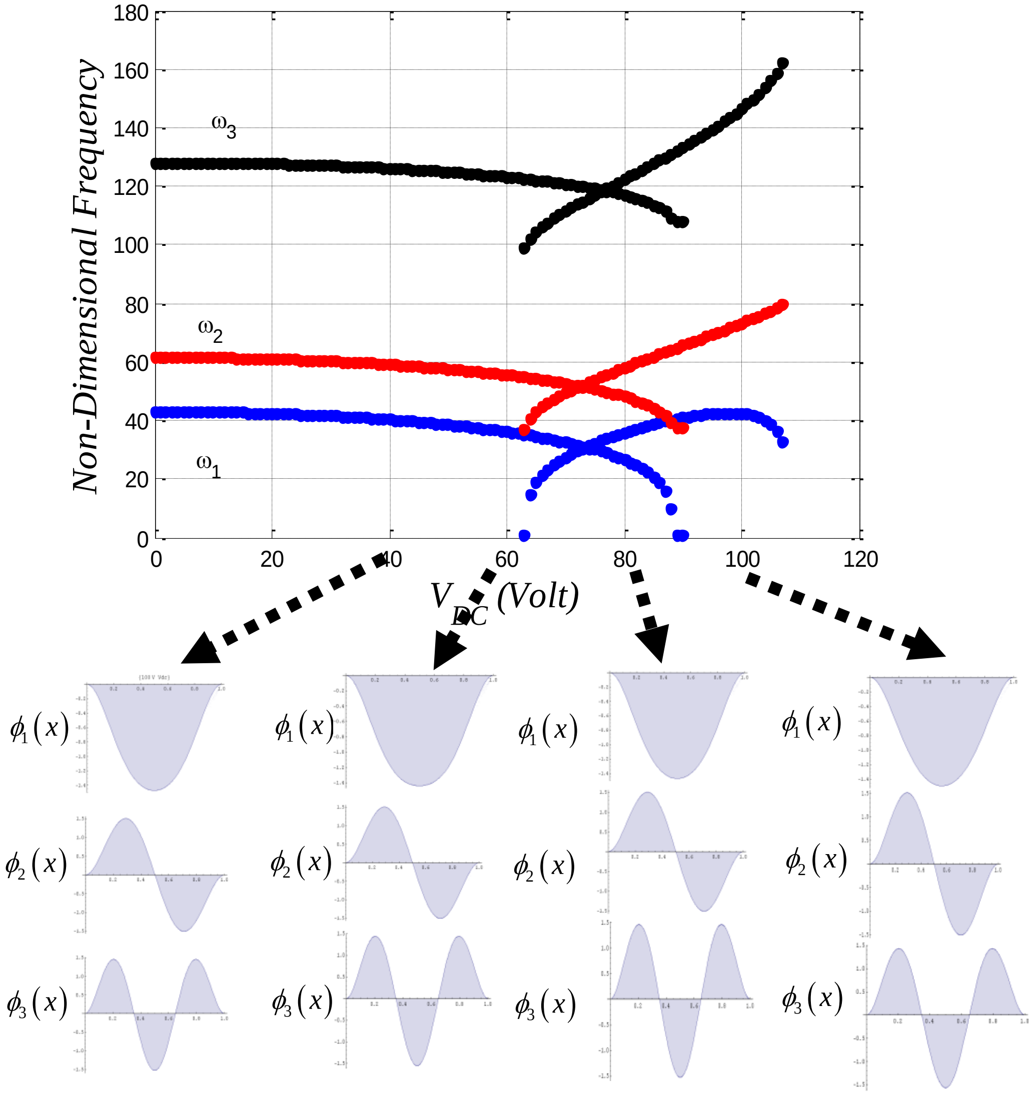

Figure 5.1: Variation of first three natural frequencies and mode shapes with V_{DC} for a parallel plate electrostatically actuated MEMS arch.

Figure 5.1 shows the variation of the first three natural frequencies of the investigated curved microbeam with DC static load. The fundamental first natural frequency goes to zero at $V_{DC} = 88$ Volts which is the occurrence of snap through instability as was depicted in the Figure 4.1. The fundamental frequency rises again beyond snap through until reaching the pull in instability where it again returns back to zero around $V_{DC} = 106$ Volts. Beyond this DC values the system collapses and the system is without stiffness. The higher natural frequencies are also shown to be sensitive to the DC voltage increase Figure 5.1 where we can see gradual decrease for the second and the third frequency up to the snap through instability beyond which there is an increase till reaching the pull in instability.

5.3 Considering Fringing Fields electrostatic MEMS Arch Actuator:

5.3.1 Eigenvalue Problem for the Case of $\hat{h} = 4.5\mu m$:

Figure 5.2 shows the variation of first three natural frequencies considering $\hat{h} = 4.5\mu m$ as the initial elevation. All the natural frequencies start to decrease prior to and in the linear region $0 \le V_{DC} \le 140$ of steep and constant slope that was discussed in the static analysis of Figure 4.2. This is due to huge softening effect in this case. If we keep increasing the DC load further, all the natural frequencies start to increase, considerably for the symmetric modes (first and third frequencies) and gradually for the anti-symmetric modes (second). These trends are highly related to the hardening effect of the microbeam in this particular DC load range. This resulted in a crossing between the first and the second frequency. There is further no decrease in the fundamental frequency for the second time as in the case of parallel plate actuation, Figure 5.1. The first fundamental frequency saturates to a constant value whereas the higher frequencies increase monotonically. This makes the first and the second frequency to cross again for the second time at higher DC voltage.

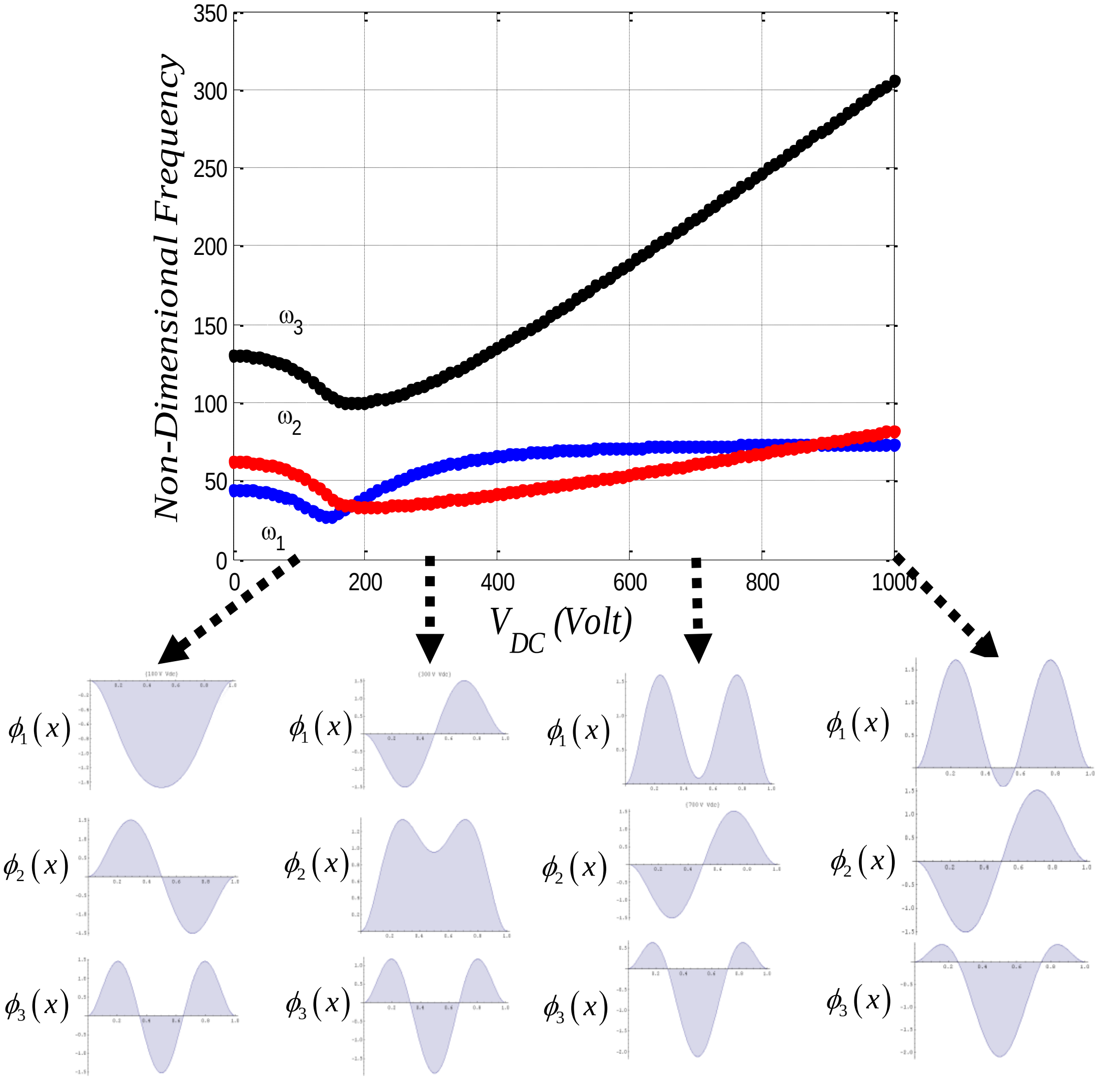

Figure 5.2: Variation of first three natural frequencies and mode shapes with V_{DC} for $h = 4.5\mu m$.

In order to elaborate more in this regard, the variation of the mode shapes associated with the mentioned natural frequencies are plotted in the same figure for various DC load. The crossing between the first (symmetric) and the second (anti-symmetric) frequencies can be observed in the representation of the respective mode shapes. It can be noticed that the first mode shape tends to attend the shape of the third mode shape for higher values of DC voltage. This is mainly due to the fact that the microbeam is not smoothly straight in its stable position but slightly distorted in the shape of the third mode eigenfunction as can be seen in the static profile depicted in Figure 4.3.

5.3.2 Eigenvalue Problem for the Case of $\hat{h} = 9\mu m$:

Figure 5.3 shows the variation of first three natural frequencies considering now a midpoint elevation of $\hat{h} = 9\mu m$. The fundamental frequency decreases to zero at the occurrence of symmetry breaking (first bifurcation) sharply. This can be also seen in the static midpoint elevation curve of Figure 4.4.

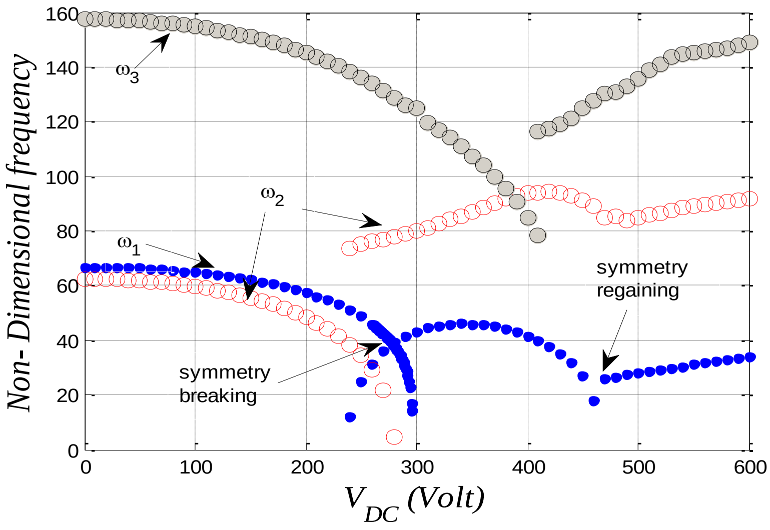

Figure 5.3: Variation of first three natural frequencies with V_{DC} for $\hat{h} = 9\mu m$.

This is similar to the behavior of parallel plate actuation case of Figure 5.1, where the fundamental frequency goes to zero when the microbeam undergoes snap-through instability. It is worth to mention that the bifurcation here is asymmetric causing the beam to lose its symmetry as discussed in the previous Chapter (Figures 4.4 and 4.5). After this first bifurcation, the fundamental frequency increases again until dropping again to zero at the voltage where the beam regains again its symmetry. Beyond that there is a continuous increase in all the frequencies. As of the asymmetric mode (the second frequency) is concerned, it also goes to zero at symmetry breaking but beyond that it sees a big jump to higher value. The second frequency dips a little at the symmetry regaining point and increases gradually beyond that bifurcation point. It is worth to be noted that the asymmetric or the second frequency is lower that the first frequency for low values of the voltages because of the high initial elevation of the microbeam. The third frequency can also be seen as sensitive to the variation of DC applied load.

5.3.3 Effect of Initial Elevation on the Fundamental Frequency:

Figure 5.4 shows the variation of the fundamental natural frequency of the curved beam actuated by fringing electric field electrostatic for various midpoint elevations $\hat{h}$ with the DC applied load. The figure shows that for $\hat{h} = 3\mu m$ and $\hat{h} = 4.5\mu m$, there is first decrease in the linear region with constant slope as discussed previously in Section 5.3.1. Beyond this region there is an increase in the fundamental frequency until it settles at a constant value when the microbeam becomes almost straight and where the net electrostatic force becomes zero. The fundamental frequency, in the case of higher microbeam initial elevation, in this case $\hat{h} = 9\mu m$, goes to zero when the beam undergoes symmetry breaking due to the asymmetric bifurcation. After this bifurcation point, the frequency rises again before going back to zero when the microbeam regains its symmetry. At higher DC load, the fundamental frequency keeps rising gradually when the microbeam tends mimic the shape of the third mode shape.

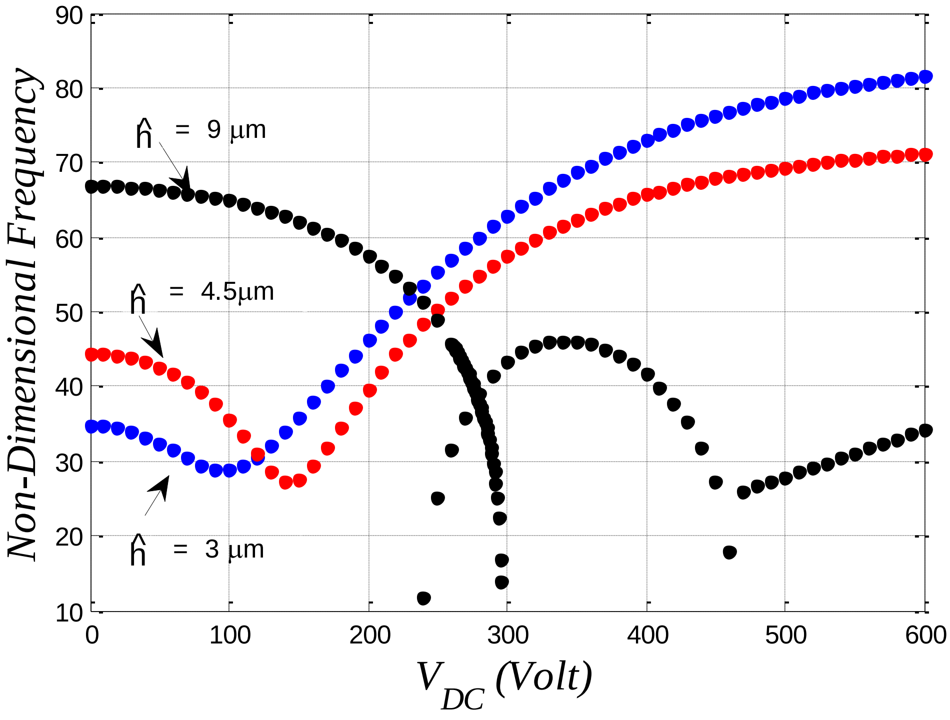

Figure 5.4: Variation of fundamental natural frequency with V_{DC} for various initial midpoint elevations $\hat{h}$.

CHAPTER 6

BIFURCATION ANALYSIS

In this Chapter we perform the bifurcation analysis for microbeams actuated by parallel plate as well as fringing field electrostatic. The criteria for symmetric as well as asymmetric bifurcation are obtained here.

6.1 Bifurcation Analysis of Parallel Plates Electrostatic Actuator

In this Section, we demonstrate the bifurcation criterion for parallel plates electrostatic microbeam actuator Figure 3.3. It is important to mention that to obtain the asymmetric bifurcation, the reduced order model (ROM) must contain at least two modes: the first symmetric and the first anti symmetric (second) mode as shown in Figure 6.1. Hence we will only use the first two modes in the ROM to study the bifurcation analysis of the actuator. Expanding the discretized system static equation for parallel plate electrostatic actuator (Equation 3.37) for the first two modes of ROM we get:

$$\int_0^1 \left[\sum_{i=1}^{2} \left\{ q_i \phi_i''''(x) \right\} \phi_1(x) \right] dx = \alpha_1 \Gamma \int_0^1 \left\{ \left(\sum_{i=1}^{2} q_i \phi_i''(x) - w_0'' \right) \phi_1(x) \right\} dx + \alpha_2 \left(V_{DC} \right)^2 \int_0^1 \frac{\phi_1(x)}{\left(1 + w_0 - \sum_{i=1}^{2} q_i \phi_i(x) \right)^2} dx, \tag{6.1a}$$

$$\int_0^1 \left[\sum_{i=1}^{2} \left\{ q_i \phi_i''''(x) \right\} \phi_2(x) \right] dx = \alpha_1 \Gamma \int_0^1 \left\{ \left(\sum_{i=1}^{2} q_i \phi_i''(x) - w_0'' \right) \phi_2(x) \right\} dx + \alpha_2 \left(V_{DC} \right)^2 \int_0^1 \frac{\phi_2(x)}{\left(1 + w_0 - \sum_{i=1}^{2} q_i \phi_i(x) \right)^2} dx, \tag{6.1b}$$

$$\forall i = 1, 2.$$

where α_1 and α_2 are given in Table 3.1.

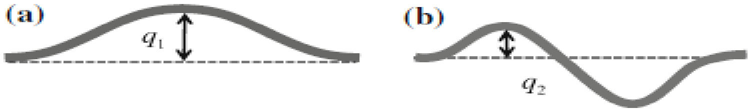

Figure 6.1: (a) First symmetric and (b) first asymmetric mode shapes.

The geometrical and material parameters for the investigated curved microbeam are summarized in Table 4.1 with only the changes mentioned in the Table below:

Table 6.1: Case study parameters for the bifurcation analysis considering parallel plates electrostatic actuation.

Height	$d = 2\mu m$
Electrode Gap	$g_0 = 10\mu m$

6.1.1 Symmetric Snap Through

Symmetric snap through criterion is obtained by neglecting the anti-symmetric mode. Hence the ROM equation reduces to one mode equation, such that:

$$\int_0^1 \left[\left\{q_1\phi_1''''(x)\right\}\phi_1(x)\right]dx = \alpha_1\Gamma\int_0^1\left[\left\{q_1\phi_1''(x)-w_0''\right\}\phi_1(x)\right]dx+\alpha_2\left(V_{DC}\right)^2\int_0^1\frac{\phi_1(x)}{\left(1+w_0-q_1\phi_1(x)\right)^2}dx, \qquad (6.2)$$

At a symmetric snap through instability there will be two different values of the curved beams midpoint elevation for a particular load or DC voltage (as can be seen in Figure 4.1). The sudden jump of the microbeam from one position to a faraway configuration is a result of the bifurcation. Therefore the variation of the voltage parameter

$\beta_{sym} = \alpha_2 \left(V_{DC}\right)^2$ with respect to the elevation is equal to zero at this point. The beam deflection $w(x)$ is a function of the mode shape $\phi_1\left(x\right)$ which is fixed for all beam elevations as well as the modal coordinate q_1 which is constant for particular elevations but vary with the change in the microbeam's position. One mode ROM will have only one static modal coordinate q_1 in this case. Hence the variation of β_{sym} with the modal coordinate q_1 should also be zero. Expressing the voltage parameter β_{sym} in terms of q_1 is:

$$\beta_{sym} = \alpha_2 \left(V_{DC}\right)^2 = \frac{1}{\int_0^1 \frac{\phi_1\left(x\right)}{\left(1 + w_0 - q_1\phi_1\left(x\right)\right)^2} dx} \left[\int_0^1 \left[\left\{ q_1\phi_1''''\left(x\right) \right\} \phi_1\left(x\right) \right] dx - \alpha_1 \Gamma \int_0^1 \left[\left\{ q_1\phi_1''\left(x\right) - w_0'' \right\} \phi_1\left(x\right) \right] dx \right], \quad (6.3)$$

and then differentiating such that

$$\frac{d\beta_{sym}}{dq_1} = 0, \quad (6.4)$$

The roots of equation (6.4) give the symmetric branches of the bifurcation. The minimum initial midpoint elevation w_0 required for snap-through is obtained by expressing w_0 in terms of q_1 from equation (6.4) and then differentiating such that $\frac{dw_0\left(q_1\right)}{dq_1} = 0$.

The Figure 6.2 shows the symmetric bifurcation criteria of a curved microbeam actuated by parallel plate electrostatics. It shows that snap through and snap back occur in the curved microbeams when the initial midpoint elevation is higher than a certain value (approximately $\hat{h} = 1.8\mu m$) whereas the pull-in occurs for all microbeams actuated by parallel plate electrostatics. The snap through and snap back criteria are not perfectly symmetric to each other about $w_{\max} = 0$ because of the presence of hysteresis.

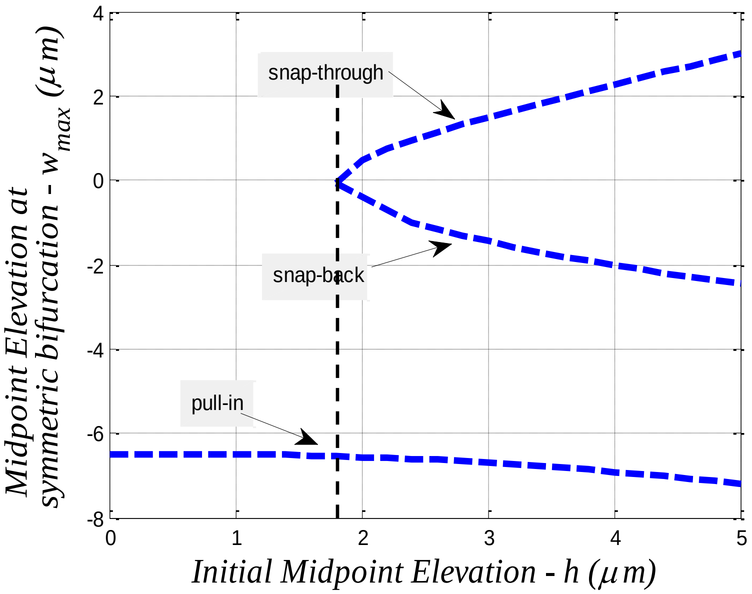

Figure 6.2: Symmetric bifurcation of curved microbeam actuated by parallel plates electrostatics.

6.1.2 Asymmetric Bifurcation

The asymmetric bifurcation criterion requires at least the first two modes in the ROM. The two static modal coordinates are q_1 and q_2. The asymmetric bifurcation criterion is obtained by firstly expressing the voltage parameter β_{asym} in terms of the modal coordinates q_1 and q_2 from Equation 6.1a such that

$$\beta_{asym} = \alpha_2 \left(V_{DC}\right)^2 = \frac{1}{\displaystyle\int_0^1 \frac{\phi_1(x)}{\left(1 + w_0 - \sum_{i=1}^{2} q_i \phi_i(x)\right)^2} dx} \left[\int_0^1 \left[\sum_{i=1}^{2} \left\{ q_i \phi_i''''(x) \right\} \phi_1(x) \right] dx - \alpha_1 \Gamma \int_0^1 \left\{ \left(\sum_{i=1}^{2} q_i \phi_i''(x) - w_0'' \right) \phi_1(x) \right\} dx \right], \quad (6.5)$$

We then substitute the obtained value of β_{asym} in to Equation 6.1b after linearizing the non-linear expression of the electrostatic force using Taylor's series expansion. This results in a linear eigenvalue problem whose non-trivial solution is found by taking into consideration the coefficient of q_2 equal to 0 as q_2 cannot be 0 for asymmetric bifurcation. The minimum initial midpoint elevation w_0 required for asymmetric bifurcation is obtained by expressing w_0 in terms of q_1 from the eigenvalue problem equation and then differentiating such that $\frac{dw_0(q_1)}{dq_1} = 0$.

Figure 6.3 shows the asymmetric snap through and asymmetric snap back for the parallel plate electrostatic actuator. The result shows that the asymmetric bifurcation occurs at an initial midpoint elevation higher than that of snap through and snap back value.

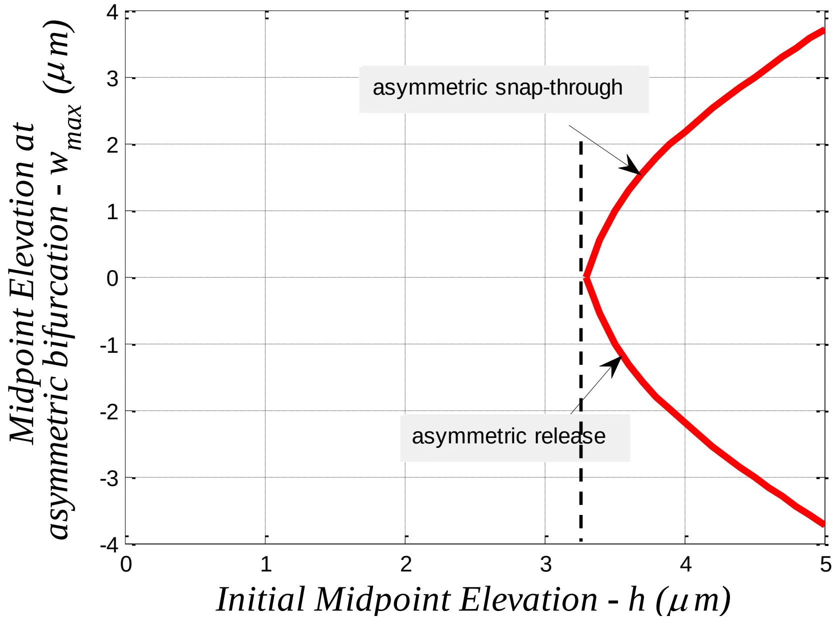

Figure 6.3: Asymmetric bifurcation of curved microbeam actuated by parallel plates electrostatics.

This clarifies more when we plotted the symmetric as well as asymmetric bifurcations together in Figure 6.4. The figure shows that the symmetric bifurcation occurs when the initial midpoint elevation is higher that a certain value (approx. $\hat{h} = 1.8\mu m$ in this case) causing the beam to undergo snap through motion. When the elevation is increased further, we start to see the occurrence of asymmetric bifurcation (at about $\hat{h} = 4\mu m$) causing symmetric breaking of the beam. (It's important to mention that the sufficient conditions for asymmetric bifurcations are met in advance ($\hat{h} = 3.4\mu m$) but practically it occurs after $\hat{h} = 4\mu m$ where the asymmetric bifurcation curves crosses over the symmetric ones. Before $\hat{h} = 4\mu m$ the deflection required for the beam to undergo symmetry breaking is higher than that needed for symmetric bifurcation. Hence the beam undergoes symmetric snap through motion to symmetrically opposite configuration and never reaches the deflection required for the occurrence of symmetry breaking.

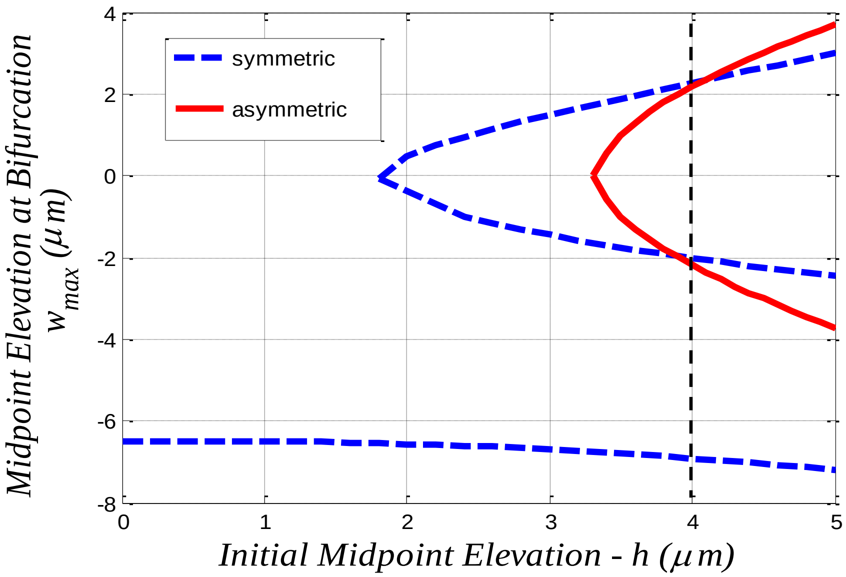

Figure 6.4: Symmetric and asymmetric bifurcations of curved microbeam actuated by parallel plates electrostatics.

6.2 Bifurcation Analysis of Fringing Fields Electrostatic Actuator Curved Microbeams

In this section we derive the bifurcation criteria of curved microbeam actuated by fringing electrostatic field Figure 3.4. The ROM static equations used in this regard and containing first two mode shapes (symmetric and anti-symmetric) are given by:

$$\begin{aligned}&\int_0^1 \left[\sum_{i=1}^{2}\left\{q_i\phi_i''''(x)\right\}\phi_1(x)\right]dx = \alpha_1\Gamma\int_0^1\left\{\left(\sum_{i=1}^{2}q_i\phi_i''(x)-w_0''\right)\phi_1(x)\right\}dx+\\ &+\alpha_2V^2\int_0^1\left\{\frac{a\sinh\left(\sigma\left(w_0-\sum_{i=1}^{2}q_i\phi_i(x)\right)\right)}{\cosh^p\left(\sigma\left(w_0-\sum_{i=1}^{2}q_i\phi_i(x)\right)\right)}H\left(x-\frac{1-0.25}{2}\right)H\left(0.25+\frac{1-0.25}{2}-x\right)\phi_1(x)\right\}dx,\end{aligned} \tag{6.6a}$$

$$\begin{aligned}&\int_0^1 \left[\sum_{i=1}^{2}\left\{q_i\phi_i''''(x)\right\}\phi_2(x)\right]dx = \alpha_1\Gamma\int_0^1\left\{\left(\sum_{i=1}^{2}q_i\phi_i''(x)-w_0''\right)\phi_2(x)\right\}dx+\\ &+\alpha_2V^2\int_0^1\left\{\frac{a\sinh\left(\sigma\left(w_0-\sum_{i=1}^{2}q_i\phi_i(x)\right)\right)}{\cosh^p\left(\sigma\left(w_0-\sum_{i=1}^{2}q_i\phi_i(x)\right)\right)}H\left(x-\frac{1-0.25}{2}\right)H\left(0.25+\frac{1-0.25}{2}-x\right)\phi_1(x)\right\}dx,\end{aligned} \tag{6.6b}$$

$$\forall i = 1, 2.$$

here α_1 and α_2 are given in Table 3.2.

The geometric and material properties of the investigated curved microbeam and actuated by fringing fields electrostatic are summarized in Table 4.2.

6.2.1 Symmetric Snap Through

The symmetric snap through criterion for this case is obtained by neglecting the anti-symmetric mode similar to the procedure described in Section 6.1.1. Hence the ROM equations (Equation 6.6a and 6.6b) simplifies to only one mode equation such that: becomes a one mode equation.

$$\begin{aligned}\int_0^1\left[\left\{q_1\phi_1''''(x)\right\}\phi_1(x)\right]dx &= \alpha_1\Gamma\int_0^1\left[\left\{q_1\phi_1''(x)-w_0''\right\}\phi_1(x)\right]dx+\\ &+\alpha_2\left(V_{DC}\right)^2\int_0^1\left\{\frac{a\sinh\left(\sigma\left(w_0-q_1\phi_1(x)\right)\right)}{\cosh^p\left(\sigma\left(w_0-q_1\phi_1(x)\right)\right)}H\left(x-\frac{1-0.25}{2}\right)H\left(0.25+\frac{1-0.25}{2}-x\right)\phi_1(x)\right\}dx,\end{aligned}\tag{6.7}$$

Where symmetric snap through occurs there will be two different values of the curved beams midpoint elevation for a particular load (DC voltage). Therefore the variation of the voltage parameter $\beta_{sym}=\alpha_2\left(V_{DC}\right)^2$ with respect to the elevation is equal to 0. Expressing the voltage parameter β_{sym} in terms of q_1, we get:

$$\beta_{sym}=\alpha_2\left(V_{DC}\right)^2=\frac{\left[\int_0^1\left[\left\{q_1\phi_1''''(x)\right\}\phi_1(x)\right]dx-\alpha_1\Gamma\int_0^1\left[\left\{q_1\phi_1''(x)-w_0''\right\}\phi_1(x)\right]dx\right]}{\int_0^1\left\{\frac{a\sinh\left(\sigma\left(w_0-q_1\phi_1(x)\right)\right)}{\cosh^p\left(\sigma\left(w_0-q_1\phi_1(x)\right)\right)}H\left(x-\frac{1-0.25}{2}\right)H\left(0.25+\frac{1-0.25}{2}-x\right)\phi_1(x)\right\}dx},\tag{6.8}$$

and then differentiating such that

$$\frac{d\beta_{sym}}{dq_1}=0,\tag{6.9}$$

The roots of Equation 6.9 provide the symmetric branches of the bifurcation. There is also an additional region where the static midpoint elevation curve exhibits a linear relationship with the applied DC load with a constant slope as was depicted and presented previously in Figure 4.2. This region can be described by the following equation:

$$\frac{d\beta_{sym}}{dq_1} = K \text{, where } K \text{ is constant.} \tag{6.10}$$

The Figure 6.5 shows the existence of two different values for a particular beam initial midpoint elevation. These refer to the snap through as well as snap back of the arch. There is no pull in for this particular actuator shape as the electrodes are located at the sides and not at the bottom of the microbeam. There is a region ($\hat{h} = 0\mu m$ to $\hat{h} = 7\mu m$) prior to the symmetric snap through shown in the Figure 6.5 representing the lower initial midpoint elevation where the slope in the static response curve, Figure 4.2 is constant. This constant slope region represents a stable range of operation through the entire range of static displacement suppressing the bi-stability nature of the microbeam. Symmetric snap through conditions are satisfied for approx. $\hat{h} > 7\mu m$.

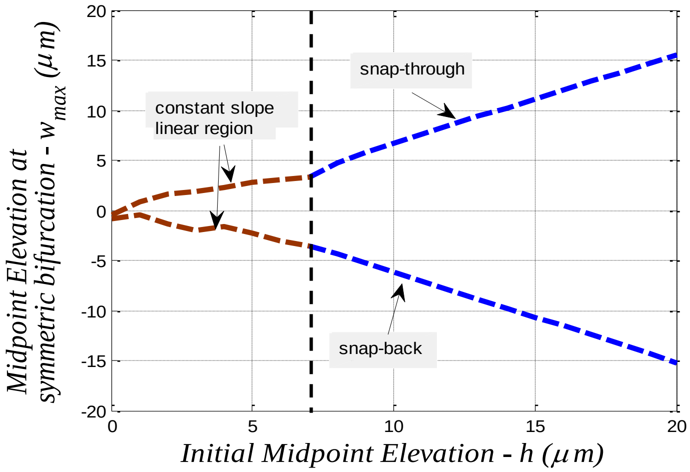

Figure 6.5: Symmetric bifurcation of curved microbeam actuated by fringing fields electrostatic.

6.2.2 Asymmetric Bifurcation

The asymmetric bifurcation criterion is derived as in Section 6.1.2 by expressing the voltage parameter β_{asym} in terms of q_1 and q_2 from Equation (6.6a), such that:

$$\beta_{asym} = \alpha_2 \left(V_{DC}\right)^2 = \frac{\left[\int_0^1 \left[\sum_{i=1}^{2} \left\{q_i \phi_i''''\left(x\right)\right\} \phi_1\left(x\right)\right] dx - \alpha_1 \Gamma \int_0^1 \left\{\left(\sum_{i=1}^{2} q_i \phi_i''\left(x\right) - w_0''\right) \phi_1\left(x\right)\right\} dx\right]}{\int_0^1 \left\{\frac{a \sinh\left(\sigma\left(w_0 - \sum_{i=1}^{2} q_i \phi_i\left(x\right)\right)\right)}{\cosh^p\left(\sigma\left(w_0 - \sum_{i=1}^{2} q_i \phi_i\left(x\right)\right)\right)} H\left(x - \frac{1-0.25}{2}\right) H\left(0.25 + \frac{1-0.25}{2} - x\right) \phi_1\left(x\right)\right\} dx}, \tag{6.11}$$

Then we substitute the β_{asym} value into Equation (6.6b) after linearizing the non-linear expression of electrostatic force using Taylor's series expansion. This results in a linear eigenvalue problem whose non-trivial solution is found by taking into consideration the coefficient of q_2 equal to zero as q_2 cannot be zero for asymmetric bifurcation.

Figure 6.6 shows that asymmetric snap through and asymmetric snap back (release) of the investigated microbeam with high initial midpoint elevation ($\hat{h} > 5\mu m$) as for the case of Figures 4.4 and 4.5. The complete bifurcation analysis of curved microbeams actuated by fringing fields electrostatic is shown in Figure 6.7 where the symmetric and asymmetric bifurcation criteria are plotted together. This figure shows that even though the criteria for symmetric bifurcations are satisfied (for $\hat{h} > 7\mu m$), the symmetric snap through and snap back never occurs for this microbeam with fringing field electrostatic actuation. The asymmetric bifurcation condition was reached ($\hat{h} > 6\mu m$) before the beam reached the necessary elevation for the initiation of symmetric bifurcation. Prior to

$\hat{h} < 6\mu m$ the microbeam has a stable range of operation throughout the range of applied load without bi-stability. The static curve for the midpoint has a linear region with constant slope in this case as in Figure 4.2.

The deflection required for asymmetric bifurcation is lesser than that needed for symmetric bifurcation with respect to the initial elevation of the microbeam. Hence the microbeam undergoes a systematic symmetric breaking without undergoing a symmetric snap through. This trend is totally different compared to what was discussed particularly for microbeam actuated by parallel plates.

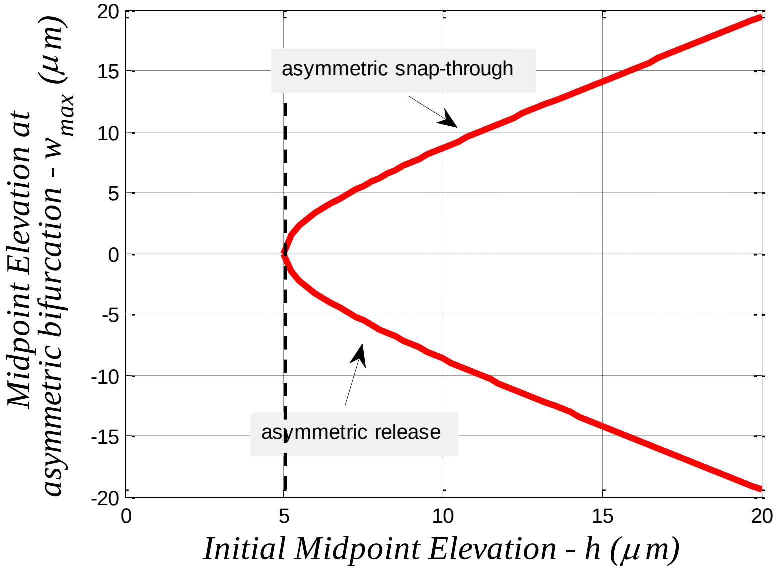

Figure 6.6: Asymmetric bifurcation of curved microbeam actuated by fringing fields electrostatic.

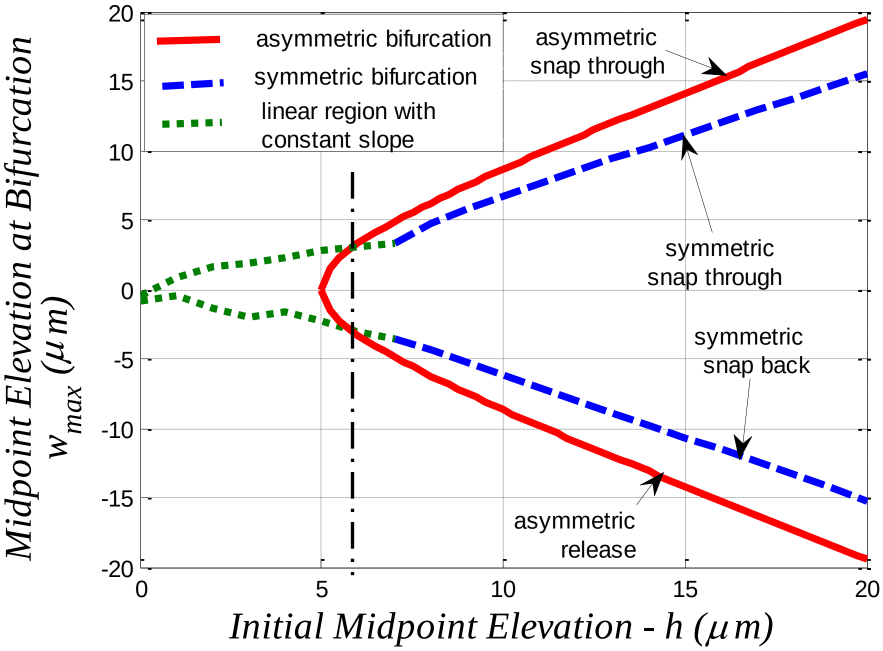

Figure 6.7: Symmetric and asymmetric bifurcation of curved microbeam actuated by fringing fields electrostatic.

The variation of the static midpoint elevation with voltage for an initial beam midpoint elevation $\hat{h} = 9\mu m$ is presented in Figure 6.8. It shows that asymmetric bifurcation (symmetry breaking) occurs before the symmetric bifurcation (snap through). The anti-symmetric mode shapes are necessary to get the asymmetric bifurcation and ascertain the occurrence of the symmetric breaking. The anti-symmetric mode shapes should not be neglected especially for arches with high initial midpoint elevation as was done previously in [32].

The static profile for $\hat{h} = 9\mu m$ without considering the anti-symmetric mode shapes are given in Figures 6.9a and 6.9b respectively. Figure 6.9a displays the occurrence of symmetric snap through whereas Figure 6.9b shows the occurrence of symmetric breaking which is more practical structural behavior of these kinds of Arches under fringing fields loads.

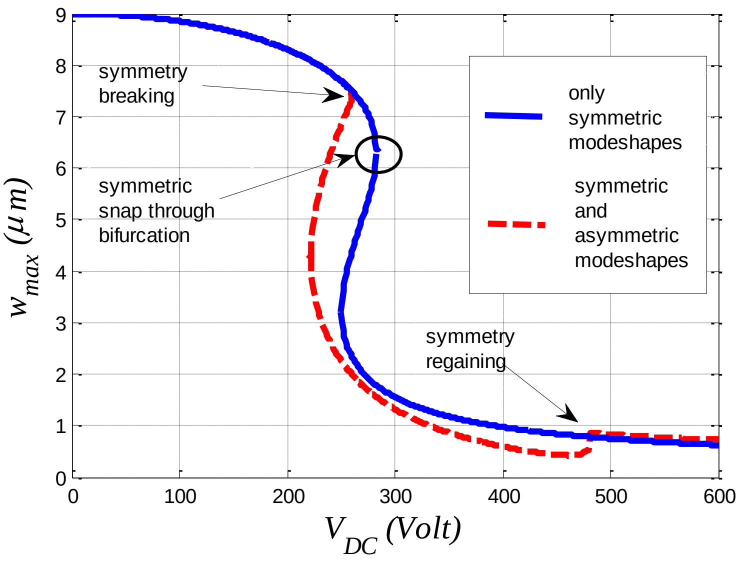

Figure 6.8: Variation of the midpoint elevation for with voltage for fringing field electrostatic actuation with and without considering the anti-symmetric mode shapes for $h = 9\mu m$.

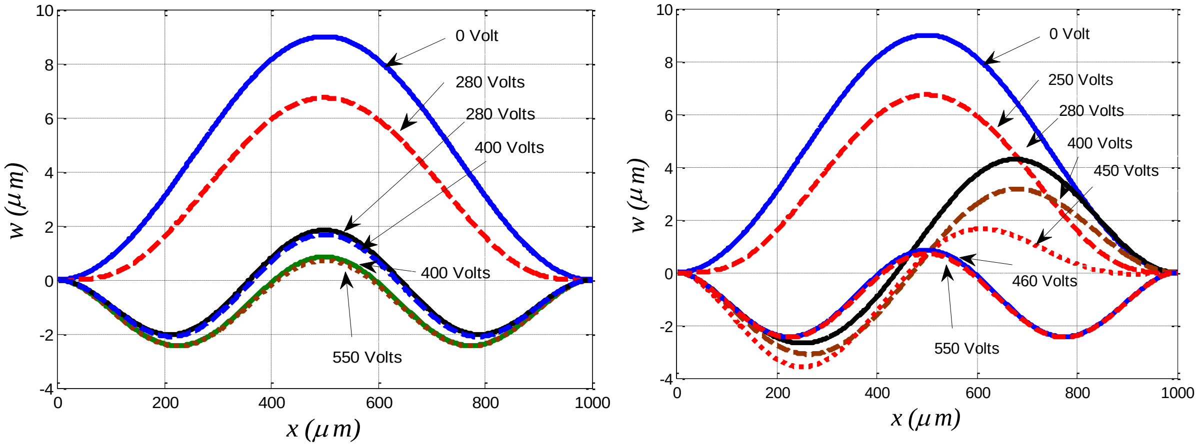

(a) (b)

Figure 6.9: Static profiles without (a) and with (b) anti-symmetric mode shapes for

$\hat{h} = 9\mu m$.

CHAPTER 7

CONCLUSIONS AND FUTURE RECOMMENDATIONS

7.1 Conclusions

Curved microbeams with low initial elevation when actuated with fringing field electrostatics demonstrate stable range of operation for the entire range of loads suppressing the bi-stability. It settles down at almost straight position for high DC load. There is linear region which has a constant slope in the midpoint displacement versus load graph.

Curved microbeams with relatively high initial elevation demonstrate bi-stability by undergoing symmetry breaking when actuated with fringing field electrostatics. Symmetry is regained back at high load when the beam tries to mimic the symmetric third mode shape.

For low elevation there is a dip in the first three frequencies at the linear region before rising again beyond it. The first frequency saturates at a certain value while the higher frequencies keep rising. There are two crossings between the first and the second frequencies.

For microbeams undergoing symmetric breaking, the first natural frequency goes to zero at symmetry breaking while the second (anti-symmetric) frequency sees a huge jump.

With increase in elevation the curved microbeams actuated by fringing electrostatic fields undergo asymmetric bifurcation directly without any symmetric snap through in between.

Anti-symmetric mode should be taken into account to see the clear picture of bifurcations especially for beams with higher elevations.

7.2 Future Recommendations

The following are recommended as an extension for future work based on the conclusions reached over this investigation:

1. A dynamic analysis can be carried out for MEMS arches actuated by fringing electrostatic fields to get the primary and secondary resonances.
2. Get the dynamic snap through criterion for the case of an AC fringing electrostatic load.
3. An internal resonance analysis can be developed to ascertain the crossing nature between the natural frequencies in the fringing-fields electrostatic actuator.
4. Develop a dynamic bifurcation and dynamic symmetry breaking criteria.
5. Perform the static and bifurcation analysis of a pre-stressed microbeam actuated by fringing electrostatic fields.

REFERENCES

[1] S. Krylov, B. R. Ilic, D. Schreiber, S. Seretensky, and H. Craighead, "The pull-in behavior of electrostatically actuated bistable microstructures," *Journal of Micromechanics and Microengineering,* vol. 18, p. 055026, 2008.

[2] L. M. Roylance and J. B. Angell, "A batch-fabricated silicon accelerometer," *Electron Devices, IEEE Transactions on,* vol. 26, pp. 1911-1917, 1979.

[3] P. F. van Kessel, L. J. Hornbeck, R. E. Meier, and M. R. Douglass, "A MEMS-based projection display," *Proceedings of the IEEE,* vol. 86, pp. 1687-1704, 1998.

[4] E. Bassous, H. H. Taub, and L. Kuhn, "Ink jet printing nozzle arrays etched in silicon," *Applied Physics Letters*, vol. 31, pp. 135-137, 1977.

[5] G. M. Rebeiz, *RF MEMS: Theory, Design, and Technology*: Wiley, 2004.

[6] S. A. Soper and W. Wang, *Bio-MEMS : technologies and applications*. Boca Raton: CRC/Taylor & Francis.

[7] E. M. Abdel-Rahman and A. H. Nayfeh, "Contact force identification using the subharmonic resonance of a contact-mode atomic force microscopy," *Nanotechnology*, vol. 16, p. 199, 2005.

[8] H. Arafat, A. Nayfeh, and E. Abdel-Rahman, "Modal interactions in contact-mode atomic force microscopes," *Nonlinear Dynamics,* vol. 54, pp. 151-166, 2008/10/01 2008.

[9] C. L. Goldsmith, Z. J. Yao, S. Eshelman, and D. Denniston, "Performance of low-loss RF MEMS capacitive switches," *Microwave and Guided Wave Letters, IEEE*, vol. 8, pp. 269-271, 1998.

[10] E. K. Chan, K. Garikipati, and R. W. Dutton, "Characterization of contact electromechanics through capacitance-voltage measurements and simulations," *Microelectromechanical Systems, Journal of,* vol. 8, pp. 208-217, 1999.

[11] M. I. Younis and A. H. Nayfeh, "A Study of the Nonlinear Response of a Resonant Microbeam to an Electric Actuation," *Nonlinear Dynamics,* vol. 31, pp. 91-117, 2003/01/01 2003.

[12] L. Liwei, R. T. Howe, and A. P. Pisano, "Microelectromechanical filters for signal processing," *Microelectromechanical Systems, Journal of,* vol. 7, pp. 286-294, 1998.

[13] J. Casals-Terre, A. Fargas-Marques, and A. M. Shkel, "Snap-Action Bistable Micromechanisms Actuated by Nonlinear Resonance," *Microelectromechanical Systems, Journal of,* vol. 17, pp. 1082-1093, 2008.

[14] J. Casals-Terre and A. Shkel, "Snap-action bistable micromechanism actuated by nonlinear resonance," in *Sensors, 2005 IEEE*, 2005, p. 4 pp.

[15] I. Z. Pane and T. Asano, "Investigation on Bistability and Fabrication of Bistable Prestressed Curved Beam," *Japanese Journal of Applied Physics,* vol. 47, p. 5291, 2008.

[16] S. Park and D. Hah, "Pre-shaped buckled-beam actuators: Theory and experiments," *Sensors and Actuators A: Physical,* vol. 148, pp. 186-192, 11/4/ 2008.

[17] V. Intaraprasonk and F. Shanhui, "Nonvolatile bistable all-optical switch from mechanical buckling," *Applied Physics Letters,* vol. 98, pp. 241104-241104-3, 2011.

[18] J. S. Go, Y.-H. Cho, B. M. Kwak, and K. Park, "Snapping microswitches with adjustable acceleration threshold," *Sensors and Actuators A: Physical,* vol. 54, pp. 579-583, 6// 1996.

[19] B. Charlot, W. Sun, K. Yamashita, H. Fujita, and H. Toshiyoshi, "Bistable nanowire for micromechanical memory," *Journal of Micromechanics and Microengineering,* vol. 18, p. 045005, 2008.

[20] R. A. M. Receveur, C. R. Marxer, R. Woering, V. C. M. H. Larik, and N. F. de Rooij, "Laterally moving bistable MEMS DC switch for biomedical applications," *Microelectromechanical Systems, Journal of,* vol. 14, pp. 1089-1098, 2005.

[21] M. I. Younis and H. M. Ouakad, "The static and dynamic behavior of MEMS arches under electrostatic actuation," in *Mechatronics and its Applications, 2009. ISMA '09. 6th International Symposium on*, 2009, pp. 1-6.

[22] J. Rossiter, B. Stoimenov, and T. Mukai, "A Self-switching Bistable Artificial Muscle Actuator," in *SICE-ICASE, 2006. International Joint Conference*, 2006, pp. 5847-5852.

[23] M. T. A. Saif, "On a tunable bistable MEMS-theory and experiment," *Microelectromechanical Systems, Journal of,* vol. 9, pp. 157-170, 2000.

[24] M. Sulfridge, T. Saif, N. Miller, and M. Meinhart, "Nonlinear dynamic study of a bistable MEMS: model and experiment," *Microelectromechanical Systems, Journal of,* vol. 13, pp. 725-731, 2004.

[25] S. Krylov, S. Seretensky, and D. Schreiber, "Pull-in behavior and multistability of a curved microbeam actuated by a distributed electrostatic force," in *Micro*

Electro Mechanical Systems, 2008. MEMS 2008. IEEE 21st International Conference on, 2008, pp. 499-502.

[26] W. E. Newell, "Miniaturization of Tuning Forks," *Science*, vol. 161, pp. 1320-1326, September 27, 1968 1968.

[27] H. C. Nathanson, W. E. Newell, R. A. Wickstrom, and J. R. Davis, Jr., "The resonant gate transistor," *Electron Devices, IEEE Transactions on*, vol. 14, pp. 117-133, 1967.

[28] Z. Yin, W. Yisong, L. Zhihong, H. Yubo, and L. Dachao, "Snap-Through and Pull-In Instabilities of an Arch-Shaped Beam Under an Electrostatic Loading," *Microelectromechanical Systems, Journal of*, vol. 16, pp. 684-693, 2007.

[29] H. M. Ouakad and M. I. Younis, "The dynamic behavior of MEMS arch resonators actuated electrically," *International Journal of Non-Linear Mechanics*, vol. 45, pp. 704-713, 9// 2010.

[30] S. Krylov and N. Dick, "Dynamic stability of electrostatically actuated initially curved shallow micro beams," *Continuum Mechanics and Thermodynamics*, vol. 22, pp. 445-468, 2010/09/01 2010.

[31] K. Das and R. C. Batra, "Pull-in and snap-through instabilities in transient deformations of microelectromechanical systems," *Journal of Micromechanics and Microengineering*, vol. 19, p. 035008, 2009.

[32] M. I. Younis, H. M. Ouakad, F. M. Alsaleem, R. Miles, and C. Weili, "Nonlinear Dynamics of MEMS Arches Under Harmonic Electrostatic Actuation," *Microelectromechanical Systems, Journal of*, vol. 19, pp. 647-656, 2010.

[33] R. C. Batra, M. Porfiri, and D. Spinello, "Electromechanical Model of Electrically Actuated Narrow Microbeams," *Microelectromechanical Systems, Journal of,* vol. 15, pp. 1175-1189, 2006.

[34] R. C. Batra, M. Porfiri, and D. Spinello, "Capacitance estimate for electrostatically actuated narrow microbeams," *Micro & Nano Letters,* vol. 1, 2006.

[35] D. Hah, P. R. Patterson, H. D. Nguyen, H. Toshiyoshi, and M. C. Wu, "Theory and experiments of angular vertical comb-drive actuators for scanning micromirrors," *Selected Topics in Quantum Electronics, IEEE Journal of,* vol. 10, pp. 505-513, 2004.

[36] V. Agache, B. Legrand, K. Nakamura, H. Kawakatsu, L. Buchaillot, H. Toshiyoshi, *et al.*, "Characterization of vertical vibration of electrostatically actuated resonators using atomic force microscope in non-contact mode," in *Solid-State Sensors, Actuators and Microsystems, 2005. Digest of Technical Papers. TRANSDUCERS '05. The 13th International Conference on,* 2005, pp. 2023-2026 Vol. 2.

[37] H. Siyuan and R. Ben Mrad, "Design, Modeling, and Demonstration of a MEMS Repulsive-Force Out-of-Plane Electrostatic Micro Actuator," *Microelectromechanical Systems, Journal of,* vol. 17, pp. 532-547, 2008.

[38] K. B. Lee, "Non-contact electrostatic microactuator using slit structures: theory and a preliminary test," *Journal of Micromechanics and Microengineering,* vol. 17, p. 2186, 2007.

[39] J. Su, H. Yang, P. Fay, W. Porod, and G. H. Bernstein, "A surface micromachined offset-drive method to extend the electrostatic travel range," *Journal of Micromechanics and Microengineering,* vol. 20, p. 015004, 2010.

[40] Y. Linzon, B. Ilic, S. Lulinsky, and S. Krylov, "Efficient parametric excitation of silicon-on-insulator microcantilever beams by fringing electrostatic fields," *Journal of Applied Physics,* vol. 113, pp. 163508-163508-11, 2013.

[41] S. Krylov, B. Ilic, and S. Lulinsky, "Bistability of curved microbeams actuated by fringing electrostatic fields," *Nonlinear Dynamics,* vol. 66, pp. 403-426, 2011/11/01 2011.

[42] M. I. Younis, E. M. Abdel-Rahman, and A. H. Nayfeh, "Global Dynamics of MEMS Resonators under Superharmonic Excitation," in *MEMS, NANO and Smart Systems, 2004. ICMENS 2004. Proceedings. 2004 International Conference on*, 2004, pp. 694-699.

[43] A. H. Nayfeh and M. I. Younis, "Dynamics of MEMS resonators under superharmonic and subharmonic excitations," *Journal of Micromechanics and Microengineering,* vol. 15, p. 1840, 2005.

[44] M. I. Younis, E. M. Abdel-Rahman, and A. Nayfeh, "A reduced-order model for electrically actuated microbeam-based MEMS," *Microelectromechanical Systems, Journal of,* vol. 12, pp. 672-680, 2003.

[45] A. Nayfeh, M. Younis, and E. Abdel-Rahman, "Reduced-Order Models for MEMS Applications," *Nonlinear Dynamics,* vol. 41, pp. 211-236, 2005/08/01 2005.

[46] Y. Feng, R. Hu, and P. Li, "A Reduced-order Model for Microbeam-based Magnetic Actuators," in *Measuring Technology and Mechatronics Automation (ICMTMA), 2011 Third International Conference on*, 2011, pp. 238-245.

[47] A. B. Pippard, "The elastic arch and its modes of instability," *European Journal of Physics,* vol. 11, p. 359, 1990.

[48] P. Patrício, M. Adda-Bedia, and M. Ben Amar, "An elastica problem: instabilities of an elastic arch," *Physica D: Nonlinear Phenomena,* vol. 124, pp. 285-295, 12/1/ 1998.

[49] C. L. Dym, *Stability theory and its applications to structural mechanics*: Noordhoff Pub., 1974.

[50] G. J. Simitses, *Dynamic stability of suddenly loaded structures*: Springer-Verlag, 1990.

[51] J. Pelesko, D. Bernstein, and J. McCuan, "Symmetry and symmetry breaking in Electrostatic MEMS," *preprint,* 2003.

[52] R. C. Batra, M. Porfiri, and D. Spinello, "Effects of Casimir force on pull-in instability in micromembranes," *EPL (Europhysics Letters),* vol. 77, p. 20010, 2007.

[53] K. Das and R. C. Batra, "Symmetry breaking, snap-through and pull-in instabilities under dynamic loading of microelectromechanical shallow arches," *Smart Materials and Structures,* vol. 18, p. 115008, 2009.

[54] L. Medina, R. Gilat, and S. Krylov, "Symmetry breaking in an initially curved micro beam loaded by a distributed electrostatic force," *International Journal of Solids and Structures,* vol. 49, pp. 1864-1876, 6/15/ 2012.

[55] L. Medina, R. Gilat, and S. Krylov, "Symmetry Breaking Criteria in Electrostatically Loaded Bistable Curved/Prebuckled Micro Beams," in *Spontaneous Symmetry Breaking, Self-Trapping, and Josephson Oscillations*. vol. 1, B. A. Malomed, Ed., ed: Springer Berlin Heidelberg, 2013, pp. 679-705.

[56] W. Hayt and J. Buck, *Engineering Electromagnetics with CD*: McGraw-Hill Companies, 2006.

[57] H. C. Nathanson and R. A. Wickstrom, "A resonant-gate silicon surface transistor with high-q band-pass properties," *Applied Physics Letters,* vol. 7, pp. 84-86, 1965.

[58] H. M. Ouakad, "Nonlinear structural mechanics of micro and nano systems," Ph.D.Dissertation, State University of New York at Binghamton, 2010.

[59] E. M. Abdel-Rahman, M. I. Younis, and A. H. Nayfeh, "Characterization of the mechanical behavior of an electrically actuated microbeam," *Journal of Micromechanics and Microengineering,* vol. 12, p. 759, 2002.

[60] H. M. Ouakad, "Static response and natural frequencies of microbeams actuated by out-of-plane electrostatic fringing-fields," *International Journal of Non-Linear Mechanics,* vol. 63, pp. 39-48, 7// 2014.

[61] D. J. Dawe, "The transverse vibration of shallow arches using the displacement method," *International Journal of Mechanical Sciences,* vol. 13, pp. 713-720, 8// 1971.

[62] A. H. Nayfeh and P. F. Pai, *Linear and Nonlinear Structural Mechanics*: Wiley, 2008.

[63] W. R. Hamilton, "On a general method in dynamics.," *Philosophical Transaction of the Royal Society Part II,* pp. 247–308, 1834.

[64] W. R. Hamilton, "On a general method in dynamics," *Philosophical Transaction of the Royal Society Part I,* pp. 95–144, 1835.

[65] H. M. Ouakad, M. I. Younis, F. M. Alsaleem, R. Miles, and W. Cui, "The static and dynamic behavior of MEMS arches under electrostatic actuation," *ASME 2009 International Design Engineering Technical Conferences and Computers and Information in Engineering Conference*, San Diego, USA, August 2009.

[66] O. Bochobza-Degani, D. Elata, and Y. Nemirovsky, "An efficient DIPIE algorithm for CAD of electrostatically actuated MEMS devices," *Microelectromechanical Systems, Journal of*, vol. 11, pp. 612-620, 2002.

VITAE

Name : TAUSIFF FIRAQUE MOHAMMAD

Nationality : INDIAN

Date of Birth : 11/10/1986

Email : tausiffzone@gmail.com

Address : Begum Villa, c/o - Md Talim, Mirdhadera, Belpahar,
Jharsuguda, Orissa, India. Pin-768 218

Academic Background :

- M.Sc Mechnaical Engineering: King Fahd University of Petroleum and Minerals (KFUPM), Dhahran, Saudi Arabia
  (GPA: 3.607 out of 4) May 2014.
- B.Tech Mechatronics Engineering: Manipal Institute of Technology, Manipal, Karnataka, India.
  (GPA: 8.21 out of 10) May 2010.

Publications :

- **Tausiff F. Mohammad** and Hassen M. Ouakad "***Static and bifurcation analysis of MEMS arches actuated by electrostatic fringing fields***",in Proc. Of the 10th IEEE/ASME International Conference on Mechatronics and Embedded Systems and Applications (MESA),Senigallia, Italy, Sept 10-12, 2014.

- **Tausiff F. Mohammad** and Hassen M. Ouakad "***Structural stability of MEMS arches actuated by electrostatic fringing fields***", International Journal of structural stability and dynamics. [To be submitted].